

CART: Compositional AutoRegressive Transformer for Image Generation

Siddharth Roheda, Rohit Chowdhury, Aniruddha Bala, Rohan Jaiswal

Samsung Research Institute

Bangalore, India

{sid.roheda, rohit.c, aniruddha.b, r.jaiswal}@samsung.com



Figure 1: Top row: Image Generation process using CART. Orange box marks generated base component. Middle Row: Generated image samples using CART. Bottom row: Applications of CART: High resolution generation without re-training (Magenta), Recoloring objects in scenes (Blue), Lighting control (Purple)

Abstract

We propose a novel Auto-Regressive (AR) image generation approach that models images as hierarchical compositions of interpretable visual layers. While AR models have achieved transformative success in language modeling, replicating this success in vision tasks remains challenging due to inherent spatial dependencies in images. Addressing the unique challenges of vision tasks, our method (CART) adds image details iteratively via semantically meaningful decompositions. We demonstrate the flexibility and generality of CART by applying it across three distinct decomposition strategies: (i) Base-Detail Decomposition (Mumford-Shah smoothness), (ii) Intrinsic Decomposition (albedo/shading), and (iii) Specularity Decomposition (diffuse/specular). This “next-detail” strategy outperforms traditional “next-token” and “next-scale” approaches, improving controllability, semantic interpretability, and resolution scalability. Experiments show CART generates visually compelling results while enabling structured image manipulation, opening new directions for controllable generative modeling via physically or perceptually motivated image factorization.

Introduction

Recent advancements in Generative AI for image synthesis have garnered significant interest across research and industry. Conventional approaches including Generative Adversarial Networks (GANs) (Goodfellow et al. 2020; Mirza 2014) and Variational Auto Encoders (VAEs) (Kingma 2013; Shao et al. 2020) typically generate entire scenes in a single pass. Recent research has introduced step-wise approaches where each step incorporates a subset of details. Diffusion-based methods (Ho, Jain, and Abbeel 2020; Song, Meng, and Ermon 2020) initiate with noise and employ denoising models to progressively reveal coherent images. Similarly, Auto-Regressive (AR) models (Van Den Oord, Kalchbrenner, and Kavukcuoglu 2016; Salimans et al. 2017; Gregor et al. 2015; Parmar et al. 2018) tackle generation in a patch-wise manner. Image generation models like VQGAN (Esser et al. 2021) and DALLE (Ramesh et al. 2021) aim to parallel the success of AR models in Large Language Modelling (LLMs) by using visual tokenizers that convert images into 2D token grids enabling next-token prediction.

Despite success of AR models in Natural Language Pro-

cessing (NLP), achieving similar vision advancements remains challenging. Recent studies in AR (Tian et al. 2024) highlight that token prediction sequence can significantly impact performance. VAR (Tian et al. 2024) adopts a multi-scale tokenization approach, where token maps at different scales are created within the encoded latent space. A transformer is then trained to predict the next higher-resolution token map, while conditioning on the previously generated token maps. This “next-scale” strategy enables progressive resolution expansion, improving upon raster-scan tokenization. However, while VAR enhances scalability, it refines both global structures and fine details simultaneously at each scale, without explicitly disentangling them. This entanglement of structural and textural features limits fine-grained control over generated image characteristics. Furthermore, such an intertwined representation necessitates retraining or fine-tuning whenever the target generation resolution deviates from that used during VAR training, limiting its flexibility across resolutions.

To address these limitations, we draw inspiration from human perception and visual content creation, which fundamentally follow a compositional approach. For instance, artists typically begin by outlining spatial layouts and global structures, then progressively refine color, textures, and details. Motivated by this process, we propose a novel compositional AR framework that synthesizes images by sequentially predicting constituent visual factors, ranging from structural layouts to appearance refinements. Our approach decomposes training images into physically relevant “base” and “detail” components, encoding them into multi-scale detail token-maps. AR processing initiates with 1×1 tokens, predicting successive token-maps to construct a base component at the target resolution. The model then predicts detail components, incrementally layering them to enhance the base image. Such a “next-detail” generation approach enables the model to synthesize images with significantly higher detail compared to state-of-the-art methods such as (Tian et al. 2024) and (Sun et al. 2024). In addition, it supports training-free high-resolution image generation and facilitates super-resolution of low-quality inputs.

The **Contributions** of this paper include:

- A novel **iterative image generation** approach aligning with natural image formation order.
- A **hierarchical tokenization strategy** to quantize an image into base and detail layers.
- **High-resolution generation and Super-Resolution without retraining**, demonstrating versatility.
- **Fine-grained control** over image characteristics such as textures, colors, and lighting.

Related Work

Generative Models

Generative models for image synthesis have advanced rapidly, enabling both unconditional and conditional generation based on priors. VAEs (Kingma 2013; Shao et al. 2020) and GANs (Goodfellow et al. 2020; Mirza 2014) established foundational approaches, with GANs generating high-quality images via adversarial training. Diffusion

models (Ho, Jain, and Abbeel 2020; Song, Meng, and Ermon 2020; Ho et al. 2022) introduce sequential denoising processes, gradually refining noise into realistic images. Their remarkable ability to synthesize high quality images with fine-grained visual details have enabled applications in text-to-image generation (Zhang et al. 2023; Zhu et al. 2023), inpainting (Lugmayr et al. 2022; Corneau, Gadde, and Martinez 2024; Yang, Chen, and Liao 2023), super-resolution (Yue, Wang, and Loy 2024; Li et al. 2022), 3D reconstruction (Anciukevičius et al. 2023; Zhou and Tuliani 2023), and image editing (Brooks, Holynski, and Efros 2023; Kawar et al. 2023; Bala et al. 2024). However, their many iterative steps add computational overhead, limiting scalability for real-time, high-resolution synthesis.

Auto-Regressive Generative Models

Auto-Regressive (AR) models attempt to predict next tokens in a sequence while conditioned on previous tokens. GPT models (Brown 2020; Radford et al. 2019) using transformers (Vaswani 2017) achieved revolutionary success in language tasks, motivating computer vision applications. Early attempts included DRAW (Gregor et al. 2015) with sequential variational auto-encoding using RNNs, and pixel-level prediction approaches (PixelCNN (Salimans et al. 2017), PixelRNN (Van Den Oord, Kalchbrenner, and Kavukcuoglu 2016), and Image Transformer (Parmar et al. 2018)). However, sequentially predicting billions of pixels proved computationally prohibitive, and Image-GPT (Chen et al. 2020) with 6.8B parameters only achieved image generation at 96×96 resolution. Vector Quantized VAE (VQ-VAE) (Van Den Oord, Vinyals et al. 2017) addressed scalability by compressing images into discrete token sequences. In (Parmar et al. 2018) transformer decoder was utilized to enable AR generation using VQ-VAE tokens. VAR (Tian et al. 2024) demonstrated that token ordering critically impacts AR image generation, and proposed multi-scale tokenization with “next-scale” prediction.

Vector Quantized VAE (VQ-VAE)

In order to perform AR modeling of images via next-token prediction, VQ-VAE is utilized to tokenize the image into discrete tokens. The encoder \mathcal{E} , converts images to feature maps $\mathbf{f} = \mathcal{E}(\mathbf{I}) \in \mathbb{R}^{h \times w \times C}$, followed by quantization to discrete tokens $\mathbf{q} = \mathcal{Q}(\mathbf{f}) \in [V]^{h \times w}$ using learnable codebook $\mathcal{Z} \in \mathbb{R}^{V \times C}$ with V vectors,

$$q^{(i,j)} = (\arg \min_{v \in [V]} \|\text{look-up}(\mathcal{Z}, v) - \mathbf{f}^{(i,j)}\|_2) \in [V], \quad (1)$$

where $\text{look-up}(\mathcal{Z}, v)$ refers to taking the v^{th} vector in codebook \mathcal{Z} . Reconstruction involves codebook lookup $\hat{\mathbf{f}} = \text{look-up}(\mathcal{Z}, \mathbf{q})$ and decoding $\hat{\mathbf{I}} = \mathcal{D}(\hat{\mathbf{f}})$. Training a VQ-VAE involves the minimization of a compound loss,

$$\|\mathbf{I} - \hat{\mathbf{I}}\|_2 + \|\mathbf{f} - \hat{\mathbf{f}}\|_2 + \lambda_p \mathcal{L}_p(\hat{\mathbf{I}}) + \lambda_G \mathcal{L}_G(\hat{\mathbf{I}}), \quad (2)$$

where \mathcal{L}_p is perceptual loss (LPIPS (Zhang et al. 2018)), \mathcal{L}_G is discriminative loss (StyleGAN (Karras, Laine, and Aila 2019)), and λ_p and λ_G are the corresponding loss weights.

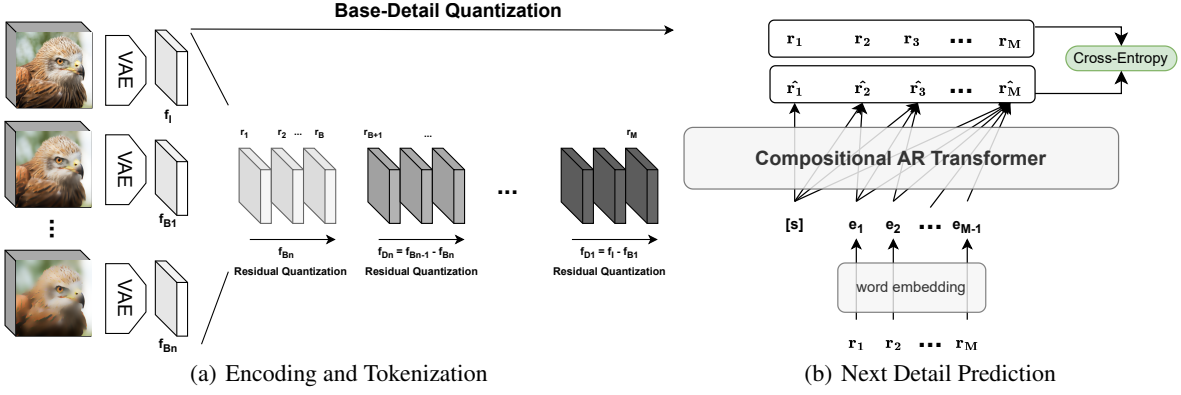


Figure 2: Overview of the CART Approach.

Mumford-Shah Functional

The Mumford-Shah functional (Mumford and Shah 1989) provides a form of all regularizers aiming at discontinuity-preserving smoothing given a bounded set $\Omega \in \mathbb{R}^d$,

$$\min_{u,K} \int_{\Omega} |u - f|^2 dx + \alpha \int_{\Omega/K} |\nabla u|^2 dx + \lambda |K|, \quad (3)$$

This approximates vector-valued input image $f : \Omega \rightarrow \mathbb{R}^k$ with function $u : \Omega \rightarrow \mathbb{R}^k$, which is smooth everywhere except at $(d-1)$ -dimensional jump set K . $\lambda > 0$ controls the length of K . A common approach to solve the Mumford-Shah functional is the Ambrosio-Tortorelli approach (1990),

$$\begin{aligned} \min_{u,s} \int_{\Omega} |u - f|^2 dx + \alpha \int_{\Omega} (1 - s)^2 |\nabla u|^2 dx \\ + \lambda \int_{\Omega} (\epsilon |\nabla s|^2 + \frac{1}{4\epsilon} s^2) dx, \end{aligned} \quad (4)$$

with a small parameter $\epsilon > 0$ and an edge set indicator $s : \Omega \rightarrow \mathbb{R}$. The points $x \in \Omega$ are part of the edge set K if $s(x) \approx 1$ and part of smooth region if $s(x) \approx 0$. The variables u and s are found by alternating minimization.

Proposed Approach

We propose a novel approach for autoregressive image generation where the model initially generates a base image focusing on global structure, and subsequently refines it through iterative detail addition. Our training methodology comprises three steps: **(1) Decomposition**: Each training image is decomposed into n hierarchical factors representing progressive detail layers, **(2) Encoding and Tokenization**: The factors are encoded into a latent space using a VQ-VAE, preserving essential features while reducing dimensionality, **(3) Iterative Prediction**: A Transformer decoder is trained to predict successive detail factors (token-maps), enabling incremental detail addition.

Hierarchical Base-Detail Decomposition

An image can be represented as a linear combination of factor images capturing distinct properties of the image. We de-

compose an image into a base and a detail factor,

$$\mathbf{I} = \mathbf{B} + \mathbf{D}, \quad (5)$$

where $\mathbf{I}, \mathbf{B}, \mathbf{D} \in \mathbb{R}^{H \times W \times 3}$ denote a training image and its corresponding base and detail factors. The base factor \mathbf{B} is obtained by minimizing the Mumford-Shah functional via the Ambrosio-Tortorelli approach, as detailed in Eq. 4. This base factor can be recursively decomposed to yield multiple detail factors,

$$\mathbf{I} = \mathbf{B}_n + \mathbf{D}_n + \mathbf{D}_{n-1} + \dots + \mathbf{D}_1, \quad (6)$$

where, $\mathbf{B}_{k-1} = \mathbf{B}_k + \mathbf{D}_k, \forall k \in \{1, \dots, n\}$. Equation 6 defines the n^{th} order decomposition of \mathbf{I} . In this decomposition, the base factor \mathbf{B}_n captures the image's overall structure, composition, and global features, while the detail factors $\{\mathbf{D}_k\}_{k=1}^n$ represent local features that contribute to the finer details of the image. Figure 4 shows the hierarchical base-detail decomposition process.

We adopt edge-aware smoothing over frequency-based decomposition methods to preserve structural integrity in base images. While frequency-domain approaches such as Discrete Cosine Transform (DCT) (Nash and et al. 2021) and Wavelet Transforms (Yu et al. 2021b) provide computational efficiency, they exhibit fundamental limitations for our compositional framework. DCT-based decomposition applies uniform smoothing across both global structures and local features, failing to distinguish between semantically important edges and fine-grained textures. Additionally, the inverse DCT/Wavelet transformation introduces ringing artifacts that compromise image quality in the reconstructed base component. In contrast, Mumford-Shah smoothing provides selective regularization that preserves global edges and large-scale structural elements while effectively smoothing textural and local features. This edge-preserving property enables successful disentanglement of structural information (captured in base factors) from fine-grained details (captured in detail factors), which is critical for our iterative refinement approach (Further discussion in supplement). Our framework maintains flexibility by supporting various image decomposition techniques within the general formulation of Equation 6. This modularity allows for domain-specific decomposition strategies while preserving the core auto-regressive generation mechanism.



Figure 3: Generated Samples using CART-256

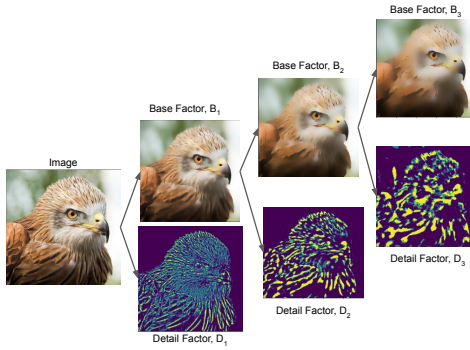


Figure 4: Hierarchical Base-Detail Decomposition

Encoding and Tokenization

In our approach, each image is represented by token maps $\{r_1, r_2, \dots, r_{\mathcal{M}}\}$ within the latent space of a Vector Quantized Variational AutoEncoder (VQ-VAE), rather than single tokens. This token-map representation preserves the spatial coherence of the feature map and reinforces the spatial structure inherent in the image. Departing from the multi-scale approach in VAR (Tian et al. 2024), we propose a tokenization scheme such that these token maps represent the base and detail factors. Specifically, the image representation is comprised of \mathcal{B} base token maps, $(r_1, \dots, r_{\mathcal{B}})$, where $\mathcal{B} < \mathcal{M}$ and $(\mathcal{M} - \mathcal{B})$ detail token maps, $(r_{\mathcal{B}+1}, \dots, r_{\mathcal{M}})$.

Following the Base-Detail Decomposition, we encode the original image I along with the Base Factors $\{\mathbf{B}_k\}_{k=1}^n$ using a VAE,

$$\mathbf{f}_{\mathbf{B}_k} = \mathcal{E}(\mathbf{B}_k), \quad (7)$$

where $\mathbf{f}_{\mathbf{B}_k} \in \mathbb{R}^{h \times w \times c} \forall k \in \{1, \dots, n\}$. The token maps representing the base factor \mathbf{B}_n , $\{r_1, \dots, r_{\mathcal{B}}\}$ are created by performing residual quantization (Lee et al. 2022) on the encoded feature map $\mathbf{f}_{\mathbf{B}_n}$ with a quantization depth of \mathcal{B} . The

encoded representation of the k^{th} detail factor is then determined as follows,

$$\mathbf{f}_{\mathbf{D}_k} = \mathbf{f}_{\mathbf{B}_{k-1}} - \mathbf{f}_{\mathbf{B}_k}, \quad (8)$$

where, $\mathbf{f}_{\mathbf{B}_k}$ is the encoded representation of the k^{th} base factor and $\mathbf{f}_{\mathbf{B}_0} = \mathbf{f}_I$. Each detail factor is quantized with quantization depth $\frac{(\mathcal{M}-\mathcal{B})}{n}$, yielding the remaining tokens, as illustrated in Figure 2(a). The full algorithm for extracting token maps from a given image is presented in Algorithm 1.

Iterative Detail Learning

We employ an auto-regressive approach to predict each successive “next-detail” token map. Given the set of tokens $\{r_1, r_2, \dots, r_{\mathcal{M}}\}$, the autoregressive likelihood is defined as,

$$P(r_1, \dots, r_{\mathcal{M}}) = \prod_{m=1}^{\mathcal{M}} P(r_m | r_1, \dots, r_{m-1}). \quad (9)$$

where each autoregressive unit, $r_m \in [V]^{h_m \times w_m}$ is a token map containing $h_m \times w_m$ tokens.

For the model architecture, we utilize a standard decoder-only Transformer architecture similar to that in GPT-2 (Radford et al. 2019), VQ-GAN (Esser et al. 2021), and VAR (Tian et al. 2024). At each auto-regressive step, the Transformer decoder predicts the distribution over all $h_m \times w_m$ tokens in parallel as depicted in Figure 2(b). To enforce causality, we apply a causal attention mask, ensuring that each token map r_m only attends to its preceding tokens $r_{\leq m}$.

Experiments

Implementation Details

For detail decomposition of training images, Mumford-Shah smoothing (Equation 4) with $\alpha = 1$, $\lambda = 0.01$ is used. Each training image is decomposed iteratively to obtain a 3rd order decomposition, $I = B_3 + D_3 + D_2 + D_1$. Note that



Figure 5: Comparison of samples generated by VAR-256 (top) and CART-256 (bottom).

Algorithm 1: Base-Detail VQ-VAE Encoding

Input:

- Raw image, I
- Target Image dimensions, $h_{\mathcal{M}}, w_{\mathcal{M}}$
- Base Image, B_n

Hyperparameters:

- Total number of tokens to represent the image, \mathcal{M}
- number of base tokens, \mathcal{B}
- number of detail factors, n

```

begin
   $f_I \leftarrow \varepsilon(I)$ 
   $f_B \leftarrow \varepsilon(B)$ 
   $f_{D_i} \leftarrow f_{B_{i-1}} - f_{B_i} \forall i \in \{1, \dots, n\}$ 
   $t \leftarrow -1$ 
  for  $k=1:\mathcal{M}$  do
    if  $k \leq \mathcal{B}$  then
       $r_k \leftarrow \mathcal{Q}(\text{interpolate}(f_B, h_k, w_k))$ 
       $R \leftarrow \text{queue}_{\text{push}}(R, r_k)$ 
       $z_k \leftarrow \text{LookUp}(r_k, \mathcal{Z})$ 
       $z_k \leftarrow \text{interpolate}(z_k, h_{\mathcal{M}}, w_{\mathcal{M}})$ 
       $f_B \leftarrow f_B - \phi_k(z_k)$ 
    end
    else
      if  $\text{mod}(k, \frac{\mathcal{M}-\mathcal{B}}{n}) = 0$  then
         $| t \leftarrow t + 1$ 
      end
       $r_k \leftarrow \mathcal{Q}(f_{D_t})$ 
       $R \leftarrow \text{queue}_{\text{push}}(R, r_k)$ 
       $z_k \leftarrow \text{LookUp}(r_k, \mathcal{Z})$ 
       $f_{D_t} \leftarrow f_{D_t} - \phi_k(z_k)$ 
    end
  end
  return base-detail tokens  $R$ .
end

```

the computational overhead due to Mumford-Shah decomposition is a one-time cost, as the decomposition is only utilized during the training process and not during inference. A Vanilla VQ-VAE (Van Den Oord, Vinyals et al. 2017) is used along with \mathcal{M} extra convolutions to realize the Base-Detail quantization scheme as depicted in Figure 2(a) and Algorithm 1. To mitigate information loss when upscaling z_k to the target resolution $h_{\mathcal{M}} \times w_{\mathcal{M}}$, we introduce an additional set of \mathcal{M} convolutional layers, denoted as $\{\phi_k\}_{k=1}^{\mathcal{M}}$ which enhance feature refinement and preserve structural details. The base and detail factors share the same code book with $V = 4096$. As in (Tian et al. 2024; Esser et al. 2021), the tokenizer is trained on OpenImages (Kuznetsova et al. 2020) with Compound loss (Equation 2) and spatial downsample of $16\times$.

Algorithm 2: Base-Detail VQ-VAE Reconstruction

Input: Base-Detail Tokens, R .

Hyperparameters:

- Total number of tokens to represent the image, \mathcal{M}
- number of base tokens, \mathcal{B}
- number of detail factors, n

```

begin
   $\hat{f} \leftarrow 0$ 
  for  $k=1:\mathcal{M}$  do
    if  $k \leq \mathcal{B}$  then
       $r_k \leftarrow \text{queue}_{\text{pop}}(R) z_k \leftarrow \text{lookup}(Z, r_k)$ 
       $z_k \leftarrow \text{interpolate}(z_k, h_k, w_k)$ 
       $\hat{f} \leftarrow \hat{f} + \phi_k(z_k)$ 
    end
    else
       $r_k \leftarrow \text{queue}_{\text{pop}}(R) z_k \leftarrow \text{lookup}(Z, r_k)$ 
       $\hat{f} \leftarrow \hat{f} + \phi_k(z_k)$ 
    end
  end
   $\hat{I} \leftarrow \mathcal{D}(\hat{f})$ 
  return reconstructed image  $\hat{I}$ 
end

```

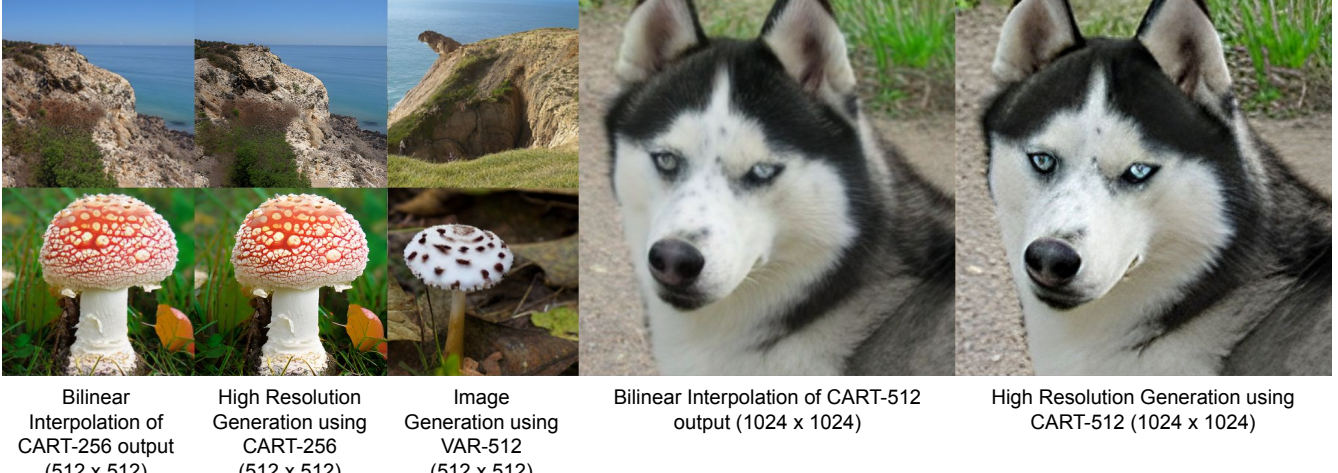


Figure 6: High Resolution image generation using patchwise detail prediction using CART-d30-256 and CART-d30-512. Zoom-in recommended to observe finer details.

The tokenized base-detail factors are then utilized to train a Transformer Decoder architecture which learns to predict the “next-detail” token. A standard decoder-only transformer architecture is used similar to GPT-2 (Radford et al. 2019) and VQGAN (Esser et al. 2021). We use a total of 14 steps to generate an image, including 8 steps to generate the base factor and 6 steps to generate the detail factors. During inference, the Transformer predicts the codes and the VQ-VAE decoder decodes the generated image. The decoding process is summarized in Algorithm 2. The depth of the transformer is varied from 16 to 30 to obtain models with varying complexity. The model is trained with initial learning rate of $1e^{-4}$. For training, we use 16 A100 GPUs with a global batch size of 768 for CART-d30-256 and batch size of 384 for CART-d30-512. All visual results are generated with seed 42 and quantitative results are averaged over 10 randomly selected seeds.

Empirical Results

The proposed CART model was evaluated on ImageNet (Deng et al. 2009) at 256×256 (CART-256) and 512×512 (CART-512) resolutions for benchmarking against SOTA image generation methods. Comparative results in Tables 1 and 2 show that CART outperforms SOTA AR and Diffusion models and achieves FID lower than ImageNet validation set while maintaining comparable complexity and generation steps. CART benefits from base-detail decomposition that disentangles global structures from local details, simplifying the learning process through more natural token ordering. Figure 3 depicts generated images using our method, while Figure 5 compares VAR (Tian et al. 2024) and CART outputs. CART produces images with enhanced details and structure compared to VAR’s “next-scale” prediction scheme. CART surpasses both Diffusion Transformer (Peebles and Xie 2023; Zhang 2024; Hatamizadeh et al. 2024) and SOTA VAR (Tian et al. 2024) in autoregressive

image generation. Extended results are provided in the supplement.

Other Applications

Generalizing to Higher Resolutions A key advantage of employing base-detail decomposition is the explicit disentanglement of global and local image features, facilitating high-resolution image synthesis and image super-resolution even when trained on lower-resolution inputs. Empirically, we observe that the base factor encapsulates global attributes, including class-conditional structure and overall color composition, while the detail factor captures local features such as textures and fine-grained details (see Figure 10). This decomposition allows the base factor to be up-scaled without loss of essential global information, while the detail factor is generated in a patchwise manner. Since the detail factor inherently lacks dependencies on global structures, patchwise synthesis does not introduce any discontinuities. Figure 6 compares bilinear upscaling and VAR (Tian et al. 2024) with our method, demonstrating that reusing lower-resolution base images and introducing patchwise details at target resolution effectively preserves content while enhancing fine details. Table 2 presents performance comparisons against state-of-the-art methods. “CART-256-NOV” refers to non-overlapping patchwise detail generation at 512×512 , while “CART-256-OV” employs 50% overlapping patches for improved continuity. “CART-512” corresponds to full training on 512×512 images. Notably, CART (trained at 256×256) outperforms VAR models trained from scratch at 512×512 . Further details and results are provided in the supplement.

Super-Resolution (SR) Given a Low-Resolution (LR) image, we encode it using Base-Detail VQVAE token maps $\{r_1, \dots, r_k\}$, where r_k has resolution $h/p \times w/p$ (h, w are LR image dimensions, p is the down-sampling factor of VQ-VAE). $\{r_1, \dots, r_k\}$ are appended as past tokens to CART’s

Type	Model	FID \downarrow	IS \uparrow	Params	Steps
GAN	BigGAN (Brock 2018)	6.95	224.5	112M	1
GAN	GigaGAN (Kang et al. 2023)	3.45	225.5	569M	1
GAN	StyleGAN-XL (Sauer et al. 2022)	2.30	265.1	166M	1
Diffusion	ADM (Dhariwal and Nichol 2021)	10.94	101.0	554M	250
Diffusion	CDM (Ho et al. 2022)	4.88	158.7	-	8100
Diffusion	LDM-4-G (Rombach et al. 2022)	3.60	247.7	400M	250
Diffusion	DiT-XL/2 (Peebles and Xie 2023)	2.27	278.2	675M	250
Diffusion	L-DiT-3B (Zhang 2024)	2.10	304.4	3.0B	250
Diffusion	L-DiT-7B (Zhang 2024)	2.28	316.2	7.0B	250
Diffusion	DiffiT (Hatamizadeh et al. 2024)	1.73	276.5	561M	250
Mask	MaskGIT (Chang et al. 2022)	6.18	182.1	227M	8
Mask	RCG (Li, Katabi, and He 2023)	3.49	215.5	502M	20
AR	VQVAE-2 (Razavi et al. 2019)	31.11	-	13.5B	5120
AR	DCTransformer (Nash and et al. 2021)	36.51	-	738M	-
AR	VQGAN-re (esser et al. 2021)	5.20	280.3	1.4B	256
AR	ViTVQ-re (Yu et al. 2021a)	3.04	227.4	1.7B	1024
AR	RQTran-re (Lee et al. 2022)	3.80	323.7	3.8B	68
AR	LlamaGen (Sun et al. 2024)	2.18	263.3	3.1B	576
AR	SpectralAR-d24 (Huang et al. 2025)	2.13	307.7	1.0B	64
VAR	VAR-d16 (Tian et al. 2024)	3.30	274.4	310M	10
VAR	VAR-d30 (Tian et al. 2024)	1.92	323.1	2B	10
VAR	VAR-d30-re (Tian et al. 2024)	1.73	350.2	2B	10
VAR	VAR-d30-re (Tian et al. 2024)	1.70	352.8	2B	14
CART	CART-d16	2.89	293.0	310M	14
CART	CART-d24	1.90	328.1	1.0B	14
CART	CART-d24-re	1.77	345.7	1.0B	14
CART	CART-d30	1.65	366.8	2.0B	14
CART	CART-d30-re	1.61	377.5	2.0B	10
CART	CART-d30-re	1.57	381.9	2.0B	14
	(val. data)	1.78	236.9		

Table 1: Quantitative results on ImageNet 256 \times 256. Suffix '-re' refers to models that use rejection sampling

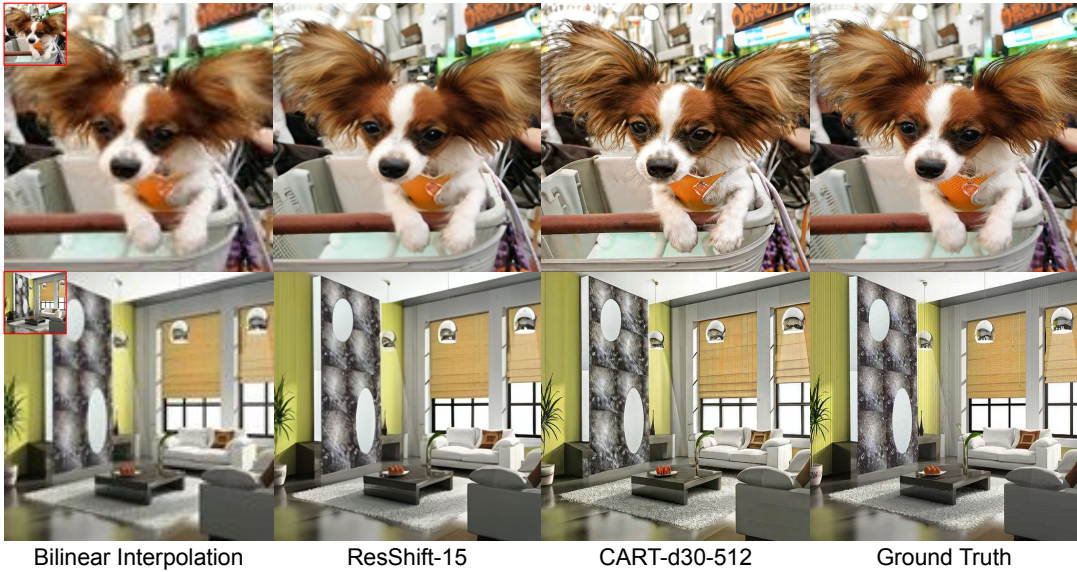


Figure 7: Comparison of CART for super-resolution with ResShift. Zoom-in recommended to observe finer details.



(a) Recoloring of generated images by manipulating albedo

(b) Recoloring of “bell-pepper” and “tent” classes

Figure 8: Recoloring of generated images when using intrinsic decomposition to tokenize the image.

Type	Model	FID \downarrow	IS \uparrow
GAN	BigGAN (2018)	8.43	177.9
Diff.	ADM (2021)	23.24	101.0
Diff.	DiT-XL/2 (2023)	3.04	240.8
Mask	MaskGiT (2022)	7.32	156.0
AR	VQGAN (2021)	26.52	66.8
VAR	VAR-d36-s (2024)	2.63	303.2
CART	CART-NOV-256-d30	2.85	297.1
CART	CART-OV-256-d30	2.54	305.7
CART	CART-512-d30	2.40	315.5

Table 2: Quantitative results on ImageNet 512 \times 512.



Figure 9: Generation using specularity decomposition. First Column: Base Diffuse Term, 2nd-5th Column: addition of specular terms to change global illumination.

prediction sequence, which then predicts subsequent token maps $\{r_{k+1}, \dots, r_M\}$ in unconditional generation setting. For target resolutions exceeding training resolution, we apply the high-resolution generation strategy described above. Table 3 compares our SR results with SOTA generative methods specifically trained or fine-tuned for super-resolution tasks and Figure 7 provides visual comparison. Although CART yields lower PSNR than ResShift (2024), it surpasses all competing methods in CLIP-IQA score (Wang, Chan, and Loy 2023), indicating superior perceptual image quality as assessed by human visual preference. Extended results are provided in the supplement.

Recoloring Generated Images Intrinsic image decomposition (Careaga and Aksoy 2023) provides a principled approach to disentangle images into reflectance (albedo) and illumination (shading) components, enabling semanti-

Model	PSNR \uparrow	SSIM \uparrow	CLIPQIA \uparrow
Real-ESRGAN (2021)	24.04	0.665	0.523
ResShift-15 (2024)	24.90	0.673	0.603
Sin-SR (2024)	24.56	0.657	0.611
CART-256-d30	24.16	0.633	0.594
CART-512-d30	24.65	0.660	0.672

Table 3: Comparison of CART models with specialized Super-Resolution models. Metrics are reported for SR from 128 \times 128 to 512 \times 512 resolution on ImageNet Test Set.

cally meaningful manipulations. CART adopts this decomposition during training to encourage controllable generation. The observed image \mathbf{I} is modeled as the composition of albedo and shading map, $\mathbf{I} = \mathbf{A} * \mathbf{S}$. Where $\mathbf{A} \in \mathbb{R}^{H \times W \times 3}$ encodes illumination-invariant properties (object color and structure) and $\mathbf{S} \in \mathbb{R}^{H \times W \times 1}$ captures illumination-dependent effects. To facilitate learning and component-wise manipulation, we convert the multiplicative decomposition to additive form via logarithmic transformation, $\log \mathbf{I} = \log \mathbf{A} + \log \mathbf{S}$. CART leverages this formulation by learning to predict the log-image and reconstructing via exponentiation, $\mathbf{I} = \exp(\log \mathbf{A} + \log \mathbf{S})$. Images are tokenized into 14 steps comprising 7 albedo and 7 shading token maps. This layered approach enables explicit learning of color and lighting factors. The decomposition and separate supervision apply only during training to induce generative factor separation. At inference, CART directly generates compositional outputs without explicit decomposition. By structurally separating these factors during training, CART supports controllable color and illumination in generated images while compositional constraints ensure globally coherent synthesis. Figure 8(a) depicts the process of image generation and color manipulation using this decomposition. Figure 8(b) depicts more instances of recoloring.

Lighting Control of Generated Images Replacing base-detail decomposition in Equation 5 with Specularity decomposition (Saini and Narayanan 2024) enables explicit lighting control in generated images. Following the dichromatic reflection model (Tominaga 1994), images consist of diffuse (\mathbf{A}) and specular (\mathbf{E}) components: $\mathbf{I} = \mathbf{A} + \mathbf{E}$. We employ 4th-order decomposition for four illumination control levels: $\mathbf{I} = \mathbf{A}_4 + \mathbf{E}_4 + \mathbf{E}_3 + \mathbf{E}_2 + \mathbf{E}_1$. Generation uses 16

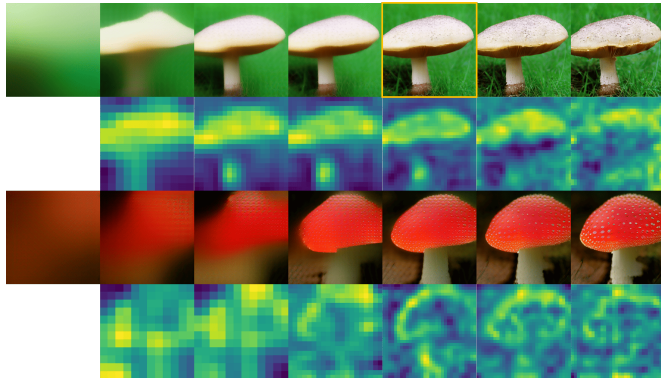


Figure 10: Top row: Intermediate visual results for CART. Base image is marked by yellow outline. 2nd row: Self-attention maps for corresponding intermediate layers of CART. 3rd row: Intermediate visual results for VAR. bottom row: Self-attention maps for corresponding intermediate layers of VAR.

Model	CFG	MS Tokens	BD Tokens	FID
AR (2021)	✗	✗	✗	18.65
VAR-d16 (2024)	✓	✓	✗	3.30
CART-d16	✓	✗	✓	2.90
CART-d16	✓	✓	✓	2.89
VAR-d30 (2024)	✓	✓	✗	1.70
CART-d30	✓	✓	✓	1.57

Table 4: Ablation Study of CART

autoregressive steps: 8 for base factor generation and 8 for controlled lighting refinement. Figure 9 demonstrates synthesized images with varying illumination while maintaining structural consistency for classes “cliff” and “volcano”. Extended results are provided in the supplement.

Ablation Study

Table 4 evaluates the impact of various CART model components. While employing multi-scale tokenization for the base factor yields only marginal gains in FID, this approach significantly reduces memory usage and accelerates generation, offering practical advantages for larger models. Table 5 compares CART performance across different decomposition orders. Decomposition order 0 is equivalent to VAR. Best performance occurs with 3rd order Base-Detail decomposition. Beyond 3rd order, the base image becomes over-smoothed and loses essential global structural details, leading to sub-optimal learning.

Figure 10 compares intermediate generations and self-attention maps for CART and VAR, the latter operating with multi-scale tokenization. VAR jointly refines global layout and local texture at each step, yielding entangled representations that hinder factor-wise control and scaling

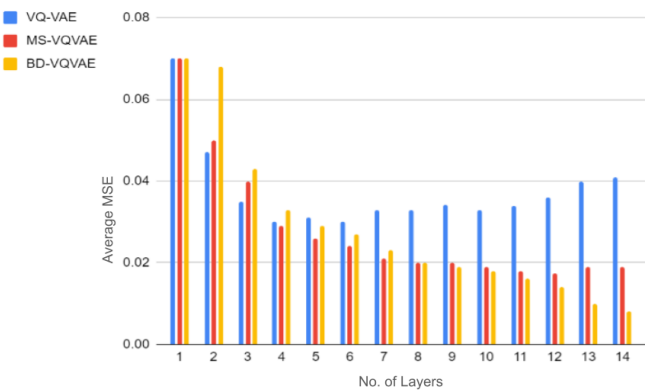


Figure 11: Reconstruction MSE of Vanilla VQ-VAE (blue), Multiscale VQ-VAE (red) and Base-Detail VQ-VAE (yellow)

Decomposition Order	FID
0 (Special case of VAR)	1.70
1	1.65
2	1.62
3	1.57
4	1.60

Table 5: Impact of decomposition order on CART model.

across resolutions. In contrast, CART first synthesizes a piecewise-smooth base capturing global structure, then incrementally adds detail factors, leading to an explicit hierarchy from structure to texture. This separation improves high-resolution synthesis via base upscaling with patch-wise detail prediction and enhances adaptability to target resolutions unseen during training. The tokenization order aligns with human perceptual organization, prioritizing coarse structures before fine details, and is reflected in progressively localized attention patterns in later steps

As shown in Figure 11, the Base-Detail VQ-VAE attains substantially lower reconstruction error than both Vanilla VQ-VAE (Yu et al. 2021a) and MS-VQ-VAE (Tian et al. 2024). Notably, while the MSE of Vanilla and MS-VQ-VAE increases at higher quantization depth, the proposed base-detail scheme continues to monotonically reduce reconstruction error, indicating more effective residual allocation and improved fidelity.

Conclusion

In this paper, we presented a novel auto-regressive framework with next-detail prediction and structured base-detail decomposition, enabling efficient, high-resolution image synthesis through iterative refinement. Our tokenization strategy of separately quantizing base and detail layers, preserves spatial integrity and enhances AR efficiency. Experiments show SOTA image generation and training-free extension to editing applications, surpassing limitations of next-token and next-scale approaches for accuracy and efficiency.

References

Ambrosio, L.; and Tortorelli, V. M. 1990. Approximation of functional depending on jumps by elliptic functional via Γ -convergence. *Communications on Pure and Applied Mathematics*, 43(8): 999–1036.

Anciukevičius, T.; Xu, Z.; Fisher, M.; Henderson, P.; Bilen, H.; Mitra, N. J.; and Guerrero, P. 2023. Renderdiffusion: Image diffusion for 3d reconstruction, inpainting and generation. In *Proceedings of the IEEE/CVF conference on computer vision and pattern recognition*, 12608–12618.

Bala, A.; Jaiswal, R.; Rashid, L.; and Roheda, S. 2024. GalaxyEdit: Large-Scale Image Editing Dataset with Enhanced Diffusion Adapter. *arXiv preprint arXiv:2411.13794*.

Brock, A. 2018. Large Scale GAN Training for High Fidelity Natural Image Synthesis. *arXiv preprint arXiv:1809.11096*.

Brooks, T.; Holynski, A.; and Efros, A. A. 2023. Instruct-pix2pix: Learning to follow image editing instructions. In *Proceedings of the IEEE/CVF Conference on Computer Vision and Pattern Recognition*, 18392–18402.

Brown, T. B. 2020. Language models are few-shot learners. *arXiv preprint arXiv:2005.14165*.

Careaga, C.; and Aksoy, Y. 2023. Intrinsic image decomposition via ordinal shading. *ACM Transactions on Graphics*, 43(1): 1–24.

Chang, H.; Zhang, H.; Jiang, L.; Liu, C.; and Freeman, W. T. 2022. Maskgit: Masked generative image transformer. In *Proceedings of the IEEE/CVF Conference on Computer Vision and Pattern Recognition*, 11315–11325.

Chen, M.; Radford, A.; Child, R.; Wu, J.; Jun, H.; Luan, D.; and Sutskever, I. 2020. Generative pretraining from pixels. In *International conference on machine learning*, 1691–1703. PMLR.

Corneanu, C.; Gadde, R.; and Martinez, A. M. 2024. Latent-paint: Image inpainting in latent space with diffusion models. In *Proceedings of the IEEE/CVF Winter Conference on Applications of Computer Vision*, 4334–4343.

Deng, J.; Dong, W.; Socher, R.; Li, L.-J.; Li, K.; and Fei-Fei, L. 2009. Imagenet: A large-scale hierarchical image database. In *2009 IEEE conference on computer vision and pattern recognition*, 248–255. Ieee.

Dhariwal, P.; and Nichol, A. 2021. Diffusion models beat gans on image synthesis. *Advances in neural information processing systems*, 34: 8780–8794.

Esser, P.; Rombach, R.; Ommer, B.; and et al. 2021. Taming transformers for high-resolution image synthesis. In *Proceedings of the IEEE/CVF conference on computer vision and pattern recognition*, 12873–12883.

Goodfellow, I.; Pouget-Abadie, J.; Mirza, M.; Xu, B.; Warde-Farley, D.; Ozair, S.; Courville, A.; and Bengio, Y. 2020. Generative adversarial networks. *Communications of the ACM*, 63(11): 139–144.

Gregor, K.; Danihelka, I.; Graves, A.; Rezende, D.; and Wierstra, D. 2015. Draw: A recurrent neural network for image generation. In *International conference on machine learning*, 1462–1471. PMLR.

Hatamizadeh, A.; Song, J.; Liu, G.; Kautz, J.; and Vahdat, A. 2024. Diffit: Diffusion vision transformers for image generation. In *European Conference on Computer Vision*, 37–55. Springer.

Ho, J.; Jain, A.; and Abbeel, P. 2020. Denoising diffusion probabilistic models. *Advances in neural information processing systems*, 33: 6840–6851.

Ho, J.; Saharia, C.; Chan, W.; Fleet, D. J.; Norouzi, M.; and Salimans, T. 2022. Cascaded diffusion models for high fidelity image generation. *Journal of Machine Learning Research*, 23(47): 1–33.

Huang, Y.; Chen, W.; Zheng, W.; Duan, Y.; Zhou, J.; and Lu, J. 2025. SpectralAR: Spectral Autoregressive Visual Generation. *arXiv preprint arXiv:2506.10962*.

Kang, M.; Zhu, J.-Y.; Zhang, R.; Park, J.; Shechtman, E.; Paris, S.; and Park, T. 2023. Scaling up gans for text-to-image synthesis. In *Proceedings of the IEEE/CVF Conference on Computer Vision and Pattern Recognition*, 10124–10134.

Karras, T.; Laine, S.; and Aila, T. 2019. A style-based generator architecture for generative adversarial networks. In *Proceedings of the IEEE/CVF conference on computer vision and pattern recognition*, 4401–4410.

Kawar, B.; Zada, S.; Lang, O.; Tov, O.; Chang, H.; Dekel, T.; Mosseri, I.; and Irani, M. 2023. Imagic: Text-based real image editing with diffusion models. In *Proceedings of the IEEE/CVF Conference on Computer Vision and Pattern Recognition*, 6007–6017.

Kingma, D. P. 2013. Auto-encoding variational bayes. *arXiv preprint arXiv:1312.6114*.

Kuznetsova, A.; Rom, H.; Alldrin, N.; Uijlings, J.; Krasin, I.; Pont-Tuset, J.; Kamali, S.; Popov, S.; Malloci, M.; Kolesnikov, A.; et al. 2020. The open images dataset v4: Unified image classification, object detection, and visual relationship detection at scale. *International journal of computer vision*, 128(7): 1956–1981.

Lee, D.; Kim, C.; Kim, S.; Cho, M.; and Han, W.-S. 2022. Autoregressive image generation using residual quantization. In *Proceedings of the IEEE/CVF Conference on Computer Vision and Pattern Recognition*, 11523–11532.

Li, H.; Yang, Y.; Chang, M.; Chen, S.; Feng, H.; Xu, Z.; Li, Q.; and Chen, Y. 2022. Srdiff: Single image super-resolution with diffusion probabilistic models. *Neurocomputing*, 479: 47–59.

Li, T.; Katabi, D.; and He, K. 2023. Self-conditioned image generation via generating representations. *arXiv preprint arXiv:2312.03701*.

Lugmayr, A.; Danelljan, M.; Romero, A.; Yu, F.; Timofte, R.; and Van Gool, L. 2022. Repaint: Inpainting using denoising diffusion probabilistic models. In *Proceedings of the IEEE/CVF conference on computer vision and pattern recognition*, 11461–11471.

Mirza, M. 2014. Conditional generative adversarial nets. *arXiv preprint arXiv:1411.1784*.

Mumford, D. B.; and Shah, J. 1989. Optimal approximations by piecewise smooth functions and associated variational problems. *Communications on pure and applied mathematics*.

Nash, C.; and et al. 2021. Generating images with sparse representations. *arXiv preprint arXiv:2103.03841*.

Parmar, N.; Vaswani, A.; Uszkoreit, J.; Kaiser, L.; Shazeer, N.; Ku, A.; and Tran, D. 2018. Image transformer. In *International conference on machine learning*, 4055–4064. PMLR.

Peebles, W.; and Xie, S. 2023. Scalable diffusion models with transformers. In *Proceedings of the IEEE/CVF International Conference on Computer Vision*, 4195–4205.

Radford, A.; Wu, J.; Child, R.; Luan, D.; Amodei, D.; Sutskever, I.; et al. 2019. Language models are unsupervised multitask learners. *OpenAI blog*, 1(8): 9.

Ramesh, A.; Pavlov, M.; Goh, G.; Gray, S.; Voss, C.; Radford, A.; Chen, M.; and Sutskever, I. 2021. Zero-shot text-to-image generation. In *International conference on machine learning*, 8821–8831. Pmlr.

Razavi, A.; Van den Oord, A.; Vinyals, O.; and et al. 2019. Generating diverse high-fidelity images with vq-vae-2. *Advances in neural information processing systems*, 32.

Rombach, R.; Blattmann, A.; Lorenz, D.; Esser, P.; and Ommer, B. 2022. High-resolution image synthesis with latent diffusion models. In *Proceedings of the IEEE/CVF conference on computer vision and pattern recognition*, 10684–10695.

Saini, S.; and Narayanan, P. 2024. Specularity factorization for low-light enhancement. In *Proceedings of the IEEE/CVF Conference on Computer Vision and Pattern Recognition*, 1–12.

Salimans, T.; Karpathy, A.; Chen, X.; and Kingma, D. P. 2017. Pixelcnn++: Improving the pixelcnn with discretized logistic mixture likelihood and other modifications. *arXiv preprint arXiv:1701.05517*.

Sauer, A.; Schwarz, K.; Geiger, A.; and et al. 2022. Stylegan-xl: Scaling stylegan to large diverse datasets. In *ACM SIGGRAPH 2022 conference proceedings*, 1–10.

Shao, H.; Yao, S.; Sun, D.; Zhang, A.; Liu, S.; Liu, D.; Wang, J.; and Abdelzaher, T. 2020. Controlvae: Controllable variational autoencoder. In *International conference on machine learning*, 8655–8664. PMLR.

Song, J.; Meng, C.; and Ermon, S. 2020. Denoising diffusion implicit models. *arXiv preprint arXiv:2010.02502*.

Sun, P.; Jiang, Y.; Chen, S.; Zhang, S.; Peng, B.; Luo, P.; and Yuan, Z. 2024. Autoregressive model beats diffusion: Llama for scalable image generation. *arXiv preprint arXiv:2406.06525*.

Tian, K.; Jiang, Y.; Yuan, Z.; Peng, B.; and Wang, L. 2024. Visual autoregressive modeling: Scalable image generation via next-scale prediction. *Advances in neural information processing systems*, 37: 84839–84865.

Tominaga, S. 1994. Dichromatic reflection models for a variety of materials. *Color Research & Application*, 19(4): 277–285.

Van Den Oord, A.; Kalchbrenner, N.; and Kavukcuoglu, K. 2016. Pixel recurrent neural networks. In *International conference on machine learning*, 1747–1756. PMLR.

Van Den Oord, A.; Vinyals, O.; et al. 2017. Neural discrete representation learning. *Advances in neural information processing systems*, 30.

Vaswani, A. 2017. Attention is all you need. *Advances in Neural Information Processing Systems*.

Wang, J.; Chan, K. C.; and Loy, C. C. 2023. Exploring clip for assessing the look and feel of images. In *Proceedings of the AAAI conference on artificial intelligence*, volume 37, 2555–2563.

Wang, X.; Xie, L.; Dong, C.; and Shan, Y. 2021. Realesrgan: Training real-world blind super-resolution with pure synthetic data. In *Proceedings of the IEEE/CVF international conference on computer vision*, 1905–1914.

Wang, Y.; Yang, W.; Chen, X.; Wang, Y.; Guo, L.; Chau, L.-P.; Liu, Z.; Qiao, Y.; Kot, A. C.; and Wen, B. 2024. Sinsr: diffusion-based image super-resolution in a single step. In *Proceedings of the IEEE/CVF conference on computer vision and pattern recognition*, 25796–25805.

Yang, S.; Chen, X.; and Liao, J. 2023. Uni-paint: A unified framework for multimodal image inpainting with pretrained diffusion model. In *Proceedings of the 31st ACM International Conference on Multimedia*, 3190–3199.

Yu, J.; Li, X.; Koh, J. Y.; Zhang, H.; Pang, R.; Qin, J.; Ku, A.; Xu, Y.; Baldridge, J.; and Wu, Y. 2021a. Vector-quantized image modeling with improved vqgan. *arXiv preprint arXiv:2110.04627*.

Yu, Y.; Zhan, F.; Lu, S.; Pan, J.; Ma, F.; Xie, X.; and Miao, C. 2021b. Wavefill: A wavelet-based generation network for image inpainting. In *Proceedings of the IEEE/CVF international conference on computer vision*, 14114–14123.

Yue, Z.; Wang, J.; and Loy, C. C. 2024. Resshift: Efficient diffusion model for image super-resolution by residual shifting. *Advances in Neural Information Processing Systems*, 36.

Zhang, C.; Zhang, C.; Zhang, M.; and Kweon, I. S. 2023. Text-to-image diffusion models in generative ai: A survey. *arXiv preprint arXiv:2303.07909*.

Zhang, R. 2024. Alpha-VLLM. Large-dit-imagenet. <https://github.com/Alpha-VLLM/LLaMA2-Accessory/tree/main/Large-DiT-ImageNet>. Accessed: 2025-07-26.

Zhang, R.; Isola, P.; Efros, A. A.; Shechtman, E.; and Wang, O. 2018. The unreasonable effectiveness of deep features as a perceptual metric. In *Proceedings of the IEEE conference on computer vision and pattern recognition*, 586–595.

Zhou, Z.; and Tulsiani, S. 2023. Sparsefusion: Distilling view-conditioned diffusion for 3d reconstruction. In *Proceedings of the IEEE/CVF Conference on Computer Vision and Pattern Recognition*, 12588–12597.

Zhu, Y.; Li, Z.; Wang, T.; He, M.; and Yao, C. 2023. Conditional text image generation with diffusion models. In *Proceedings of the IEEE/CVF Conference on Computer Vision and Pattern Recognition*, 14235–14245.

Supplementary: CART: Compositional Auto Regressive Transformer for Image Generation

Metric Definitions

Here we formally define the metrics utilized to evaluate our approach against other SOTA techniques:

- **Fréchet Inception Distance (FID ↓):** FID is a quantitative metric used to assess the quality of images generated by probabilistic models. FID measures the similarity between the distributions of features extracted from real and generated images using the Inception v3 network. Let $\mathcal{X}_{\text{real}} = \{x_i\}_{i=1}^N$ be a set of real images, $\mathcal{X}_{\text{gen}} = \{\tilde{x}_i\}_{i=1}^M$ be a set of generated images, and $f(\cdot)$ denote the feature extraction function of the Inception v3 network. Define the empirical means and covariances of the extracted features as μ_r and Σ_r for X_{real} and μ_g and Σ_g for X_{gen} . The FID between the real and generated image sets is then defined as,

$$\text{FID}^2 = \|\mu_r - \mu_g\|_2^2 + \text{Tr} \left(\Sigma_r + \Sigma_g - 2(\Sigma_r \Sigma_g)^{\frac{1}{2}} \right) \quad (10)$$

where $\|\cdot\|_2$ is the Euclidean norm, $\text{Tr}(\cdot)$ denotes the matrix trace, and $(\Sigma_r \Sigma_g)^{\frac{1}{2}}$ is the unique positive semi-definite square root of the matrix product $\Sigma_r \Sigma_g$.

A lower FID indicates a closer match between generated and real image distributions in the Inception feature space, thus reflecting better generative model quality.

- **Inception Score (IS ↑):** The Inception Score (IS) is a widely used metric for evaluating the quality and diversity of images generated by a generative model. It uses a pretrained image classification network (typically Inception v3) to assess the generated samples. Let $\mathcal{X}_{\text{gen}} = \{x_i\}_{i=1}^N$ be a set of generated images, $p(y|x)$ denote the conditional label distribution predicted by the Inception v3 model for image x , where y indexes the class labels and $p(y) = \frac{1}{N} \sum_{i=1}^N p(y|x_i)$ be the marginal distribution of predicted labels over all generated images. The Inception Score is defined as,

$$\text{IS} = \exp \left(\mathbb{E}_{x \sim \mathcal{X}_{\text{gen}}} [D_{\text{KL}}(p(y|x) \| p(y))] \right), \quad (11)$$

where $D_{\text{KL}}(\cdot \| \cdot)$ is the Kullback–Leibler divergence, and $\mathbb{E}_{x \sim \mathcal{X}_{\text{gen}}} [\cdot]$ denotes expectation over generated images.

A higher Inception Score reflects that generated images are both *highly classifiable* (each image has low-entropy, confident predictions) and *diverse* across classes (high entropy for the marginal distribution), indicating good generative model performance.

- **CLIP Image Quality Assessment Score (CLIPQA ↑):** The CLIP Image Quality Assessment Score (CLIPQA) is a no-reference image quality metric that leverages the joint multimodal embedding space of the CLIP (Contrastive Language-Image Pretraining) model for perceptual image quality assessment. It measures image quality by comparing the similarity between an image and carefully designed quality-related textual prompts within the CLIP embedding space. Let I be the input image, T_1 and T_2 be a pair of antonym text prompts (e.g., “Good photo.” and “Bad photo.”), and $x = E_{\text{img}}(I)$ be the normalized CLIP image embedding of I . Further, let $t_i = E_{\text{text}}(T_i)$ be the normalized CLIP text embedding of prompt T_i , for $i \in \{1, 2\}$. The cosine similarity between x and t_i is calculated as $s_i = x^\top t_i$. Finally, the CLIPQA score for image I is computed as,

$$\bar{s} = \frac{\exp(s_1)}{\exp(s_1) + \exp(s_2)}. \quad (12)$$

A higher CLIPQA score \bar{s} indicates that the image I aligns more closely with the positive attribute in the CLIP embedding space, reflecting better perceptual quality, aesthetics, or specified abstract properties.

- **Peak Signal to Noise Ratio (PSNR ↑):** PSNR is a widely used metric to evaluate the quality of a reconstructed image relative to a reference original. It quantifies the ratio between the maximum possible pixel value and the mean squared error (MSE) introduced by reconstruction. Let I be the original image and I_R be the reconstructed image, both of size $m \times n$. The *mean squared error* is defined as, $\text{MSE} = \frac{1}{mn} \sum_{i=0}^{m-1} \sum_{j=0}^{n-1} (I(i, j) - I_R(i, j))^2$. The PSNR, expressed in decibels (dB), is calculated as,

$$\text{PSNR} = 20 \cdot \log_{10} \left(\frac{\text{MAX}_I}{\sqrt{\text{MSE}}} \right). \quad (13)$$

A higher PSNR indicates better reconstruction quality with less distortion.

- **Structural Similarity (SSIM ↑):** SSIM is a perceptual metric used to quantify the similarity between two images, typically a reference image x and a test image y . SSIM measures image quality by considering changes in structural information while incorporating luminance and contrast masking, which aligns well with human visual perception. SSIM considers luminance similarity, $l(x, y) = \frac{2\mu_x \mu_y + C_1}{\mu_x^2 + \mu_y^2 + C_1}$, contrast similarity, $c(x, y) = \frac{2\sigma_x \sigma_y + C_2}{\sigma_x^2 + \sigma_y^2 + C_2}$, and structural similarity $s(x, y) = \frac{\sigma_{xy} + C_3}{\sigma_x \sigma_y + C_3}$. Where μ_x, μ_y are the mean intensities, σ_x, σ_y are standard deviations, and σ_{xy} is the covariance of x and y . Constants C_1, C_2, C_3 stabilize divisions to avoid instability when denominators are close to zero. The SSIM index is computed as a multiplicative combination of these components, $\text{SSIM}(x, y) = [l(x, y)]^\alpha \cdot [c(x, y)]^\beta \cdot [s(x, y)]^\gamma$. The SSIM value ranges from 0 to 1, with 1 indicating perfect structural similarity.

Analysis of Smoothing Functions for Base-Detail Decomposition

In this section, we present a comparative analysis of several candidate smoothing functions for base-detail decomposition as defined in Equation 6. Figure 12 illustrates hierarchical smoothing results obtained via five distinct smoothing techniques along with their corresponding edge maps. For each smoothing level B_k , hyper-parameters are calibrated such that all methods achieve equivalent peak signal-to-noise ratio (PSNR) values, ensuring a fair and consistent comparison. Figure 13 quantifies ringing artifacts and gradient stability across the eight smoothing levels visualized in Figure 12. As evident from the comparisons in Figure 12, Mumford–Shah smoothing yields a piecewise-smooth solution, which provides several critical advantages in the training of CART:

- **Explicit Structural-Textural Disentanglement:** Mumford–Shah smoothing facilitates a clear separation between global structures and local details. This is verifiable in the edge maps progressing from $B_8 \rightarrow B_1$ in Figure 12, where early edge maps predominantly capture major structural edges while finer details progressively emerge at later stages. Such hierarchical decomposition aligns well with the “next-detail” prediction paradigm central to CART. In contrast, alternative methods like discrete cosine transform (DCT), bilinear downsampling, and Gaussian blurring exhibit more uniform smoothing, resulting in entanglement of global and local features at each smoothing level.
- **Artifact Suppression:** The Mumford–Shah functional’s enforcement of piecewise-smoothness effectively mitigates ringing artifacts, which are prominent in DCT and wavelet-based smoothing due to the Gibbs phenomenon. Visual evidence of these ringing effects is presented in Figure 12, while their quantitative assessment in Figure 13(a) demonstrates Mumford–Shah smoothing’s superiority in minimizing such artifacts. This clean base layer decomposition enhances training stability and supports training-free high-resolution image generation and super-resolution tasks.
- **Gradient Stability:** Owing to its inherent piecewise-smooth formulation, Mumford–Shah smoothing achieves superior gradient stability compared to competing smoothing approaches (see Figure 13(b)), enabling more precise and accelerated model convergence and resulting in highly detailed, artifact-free image synthesis.
- **Reduced Reconstruction Error:** Empirical evaluation reveals that the Mumford–Shah based Base-Detail VQ-VAE outperforms multi-scale VQ-VAE in reconstruction fidelity, particularly at increased residual quantization depths (see Figure 14).

Computation of Ringing Artifact Score: The ringing artifact score quantifies oscillatory distortions near edges in the smoothed base layer. A higher score corresponds to more pronounced ringing. For a given smoothed base layer I_s and original image I , the computation proceeds as follows:

1. Detect strong edges (top 20%) in original image using sobel filter, I_E .
2. Dilate obtained edge mask to include surrounding region which is candidate region for ringing, I_D .
3. Calculate difference between Original and smooth base, $I_{Diff} = I - I_s$.
4. Compute three measures of ringing:
 - (a) Apply High-Pass filter to the difference image in order to detect high-frequency oscillations and compute standard deviation around relevant edges, $L_{HP} = stddev(HP(L_{Diff})[I_D])$
 - (b) Apply FFT to convert difference image to frequency domain, and compute difference in frequency domain for mid to high range frequencies, $L_{FFT} = mean(FFT(I_{Diff})[FreqMask])$
 - (c) Calculate variance around edges in neighboring pixels, $L_{var} = mean(var(I_{Diff})[I_D])$
5. Compute final ringing score, $L_{ringing} = \alpha * L_{HP} + \beta * L_{FFT} + \gamma * L_{var}$.

Computation of Gradient Stability Scores: The gradient stability score assesses the preservation of image gradients in the smoothed base layer. A higher value indicates better gradient preservation. Given the original image I and smoothed base I_s :

1. Calculate the gradients of original image, $I_G = grad(I)$ and the base layer, $I_{s_G} = grad(I_s)$.
2. Calculate the gradient stability score as the Pearson correlation coefficient between I_G and I_{s_G} , $L_{Gradient} = Corr(I_G, I_{s_G})$.

This rigorous evaluation substantiates Mumford–Shah smoothing as the preferred approach for base-detail decomposition within CART, balancing structural clarity, artifact mitigation, and gradient stability, thereby enhancing downstream autoregressive modeling and reconstruction fidelity.



Figure 12: Hierarchical smoothing using five different techniques. Zoom in recommended to observe fine details.

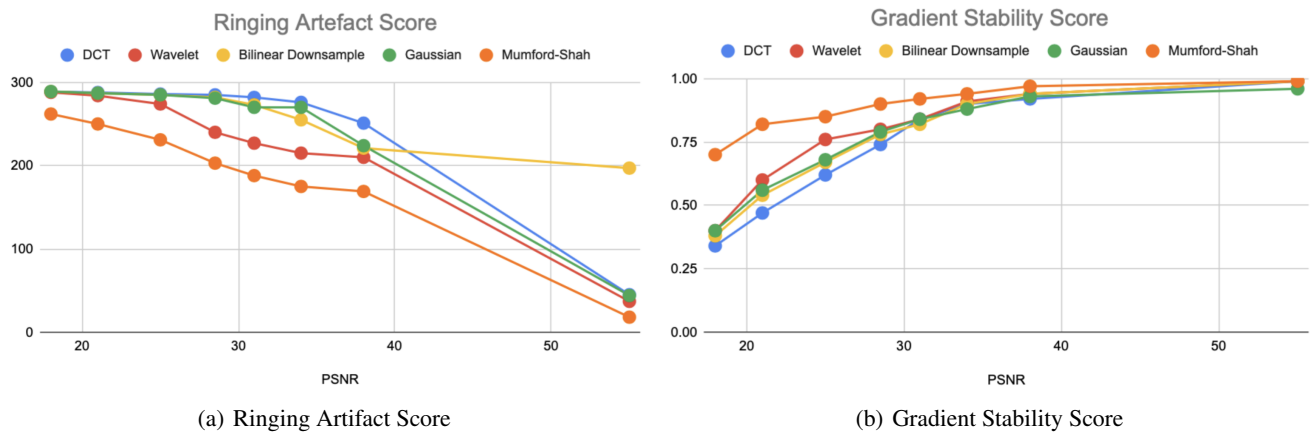


Figure 13: Ringing and Gradient Stability scores across the 8 levels depicted in Figure 12

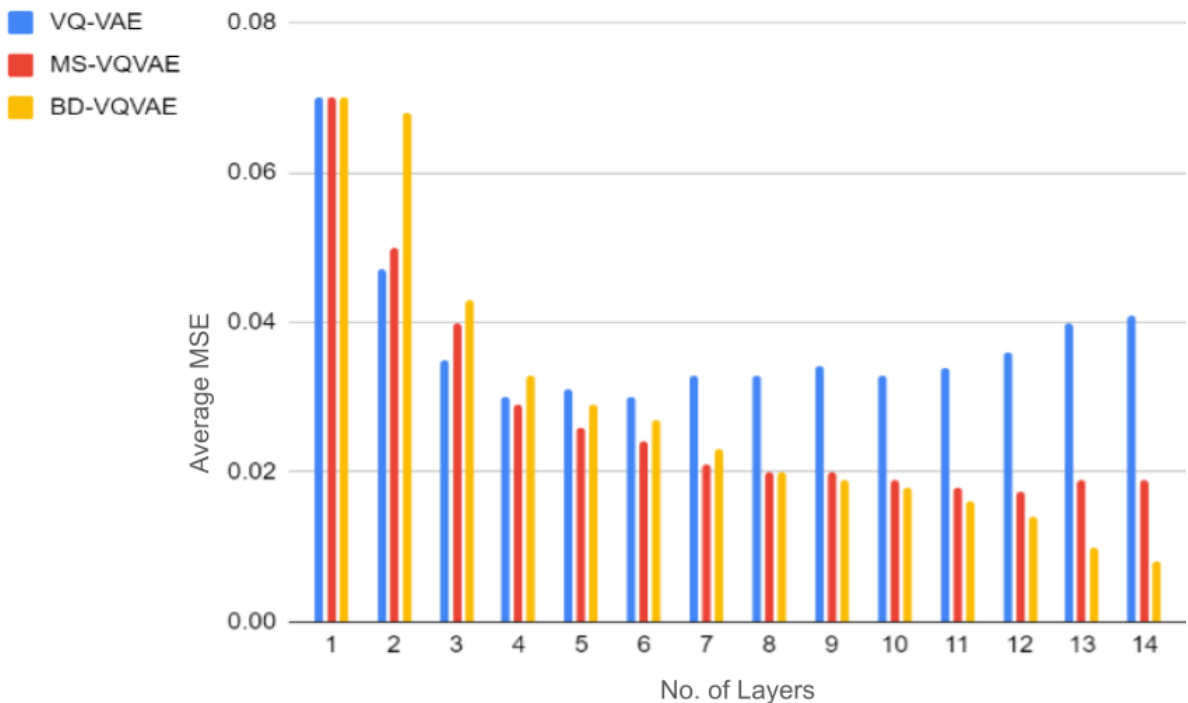


Figure 14: Reconstruction MSE of Vanilla VQ-VAE (blue), Multiscale VQ-VAE (red) and Base-Detail VQ-VAE (yellow)

Extended Results

Figures 15 - 20 cover some generations from the CART model. These generations show the diversity of the CART model and how it generalizes over many classes while producing samples with enhanced details.



Figure 15: Generated Samples using CART



Figure 16: Generated Samples using CART



Figure 17: Generated Samples using CART



Figure 18: Generated Samples using CART



Figure 19: Generated Samples using CART



Figure 20: Generated Samples using CART

High Resolution Image Generation

The approach discussed in section can be used to generate high-resolution images without any retraining of the base model as depicted in Figure 21. In Figures 22 and 23 we depict the generation of images at resolutions 1024×1024 and 2048×2048 using the CART-d30 model trained at 512×512 model. Note that we are capable of maintaining the same image content as the low resolution image as we re-use the base image generated at the lower resolution and only introduce patch-wise details at the desired higher-resolution.

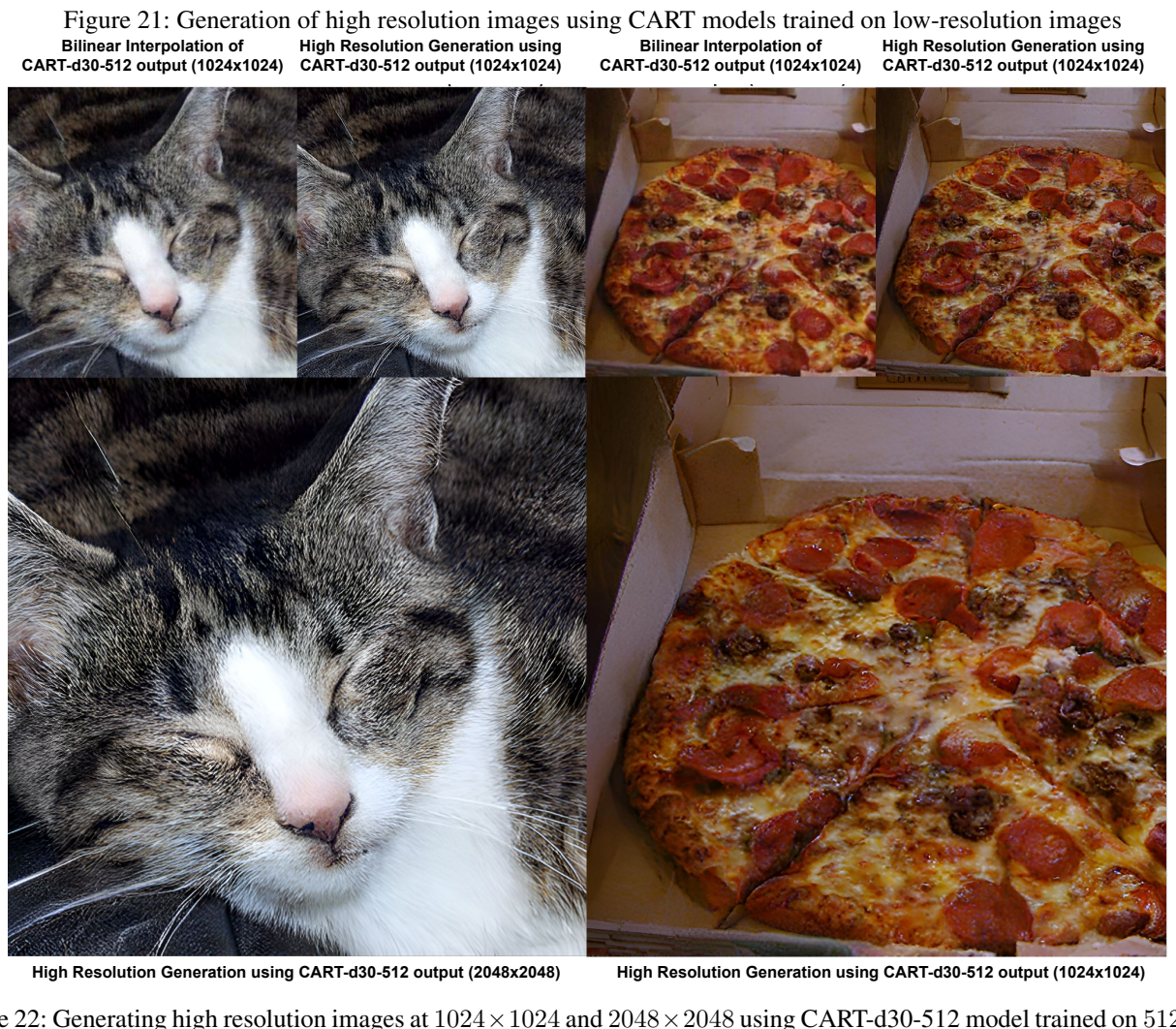
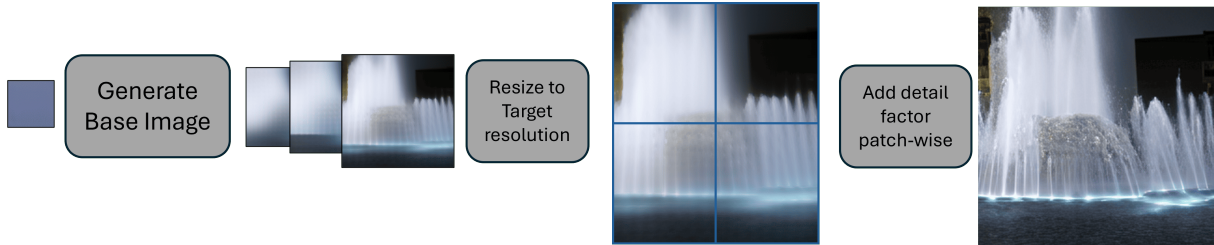


Figure 22: Generating high resolution images at 1024×1024 and 2048×2048 using CART-d30-512 model trained on 512×512 resolution. Left: Cat; Right: Pizza



Figure 23: Generating high resolution images at 1024×1024 and 2048×2048 using CART-d30-512 model trained on 512×512 resolution. Left: Espresso; Right: Teddy

Extended Results for Image Super-Resolution Using CART

Figures 24 through 28 present the results of image super-resolution achieved using the CART-d30-512 model. The visual comparisons clearly demonstrate that CART-d30-512 produces images with enhanced textures and superior perceptual quality compared to those generated by the diffusion-based ResShift-15 method.

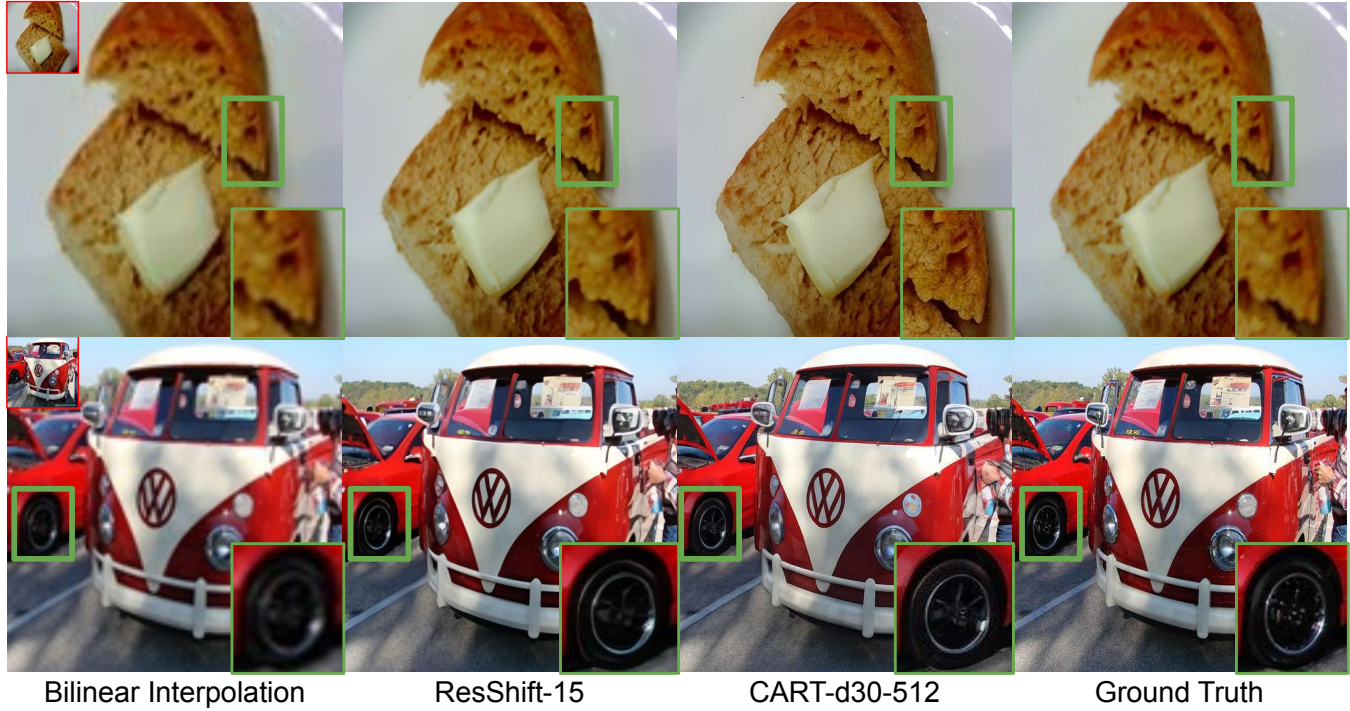


Figure 24: Comparison of CART for super-resolution with ResShift. Zoom-in recommended to observe finer details.

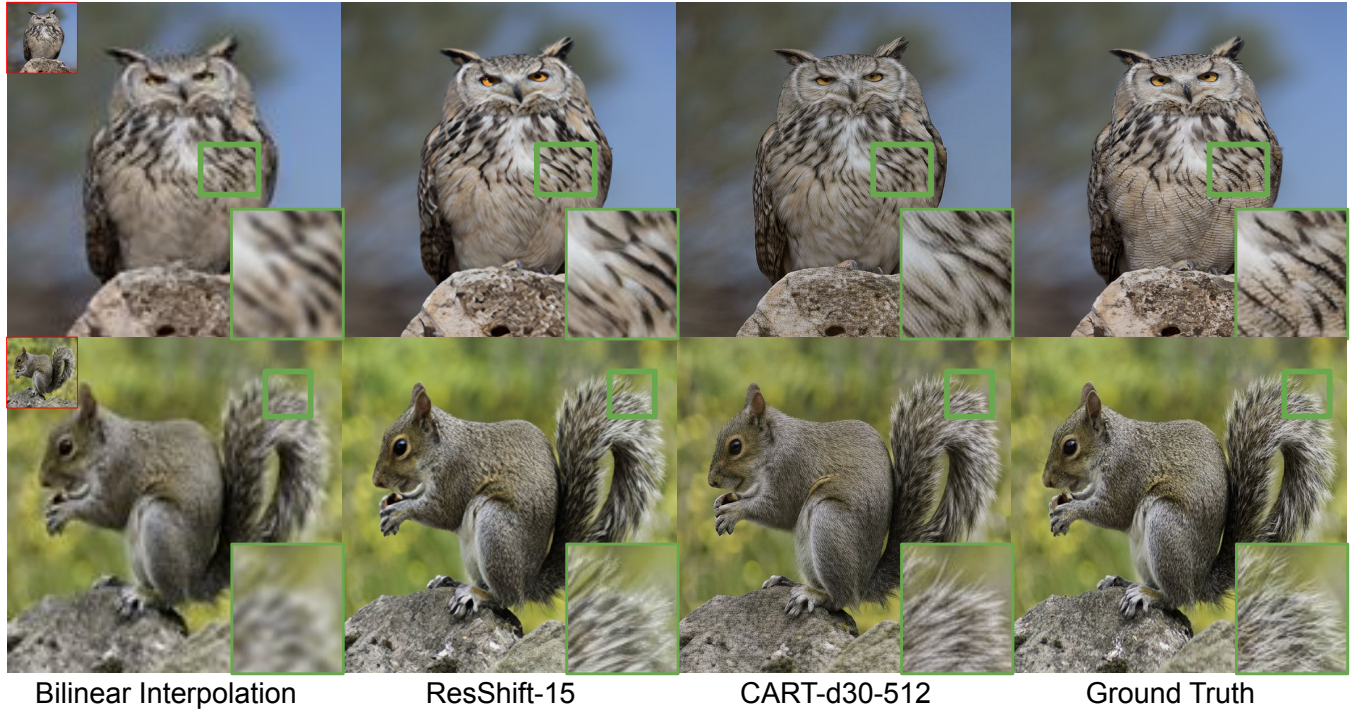


Figure 25: Comparison of CART for super-resolution with ResShift. Zoom-in recommended to observe finer details.

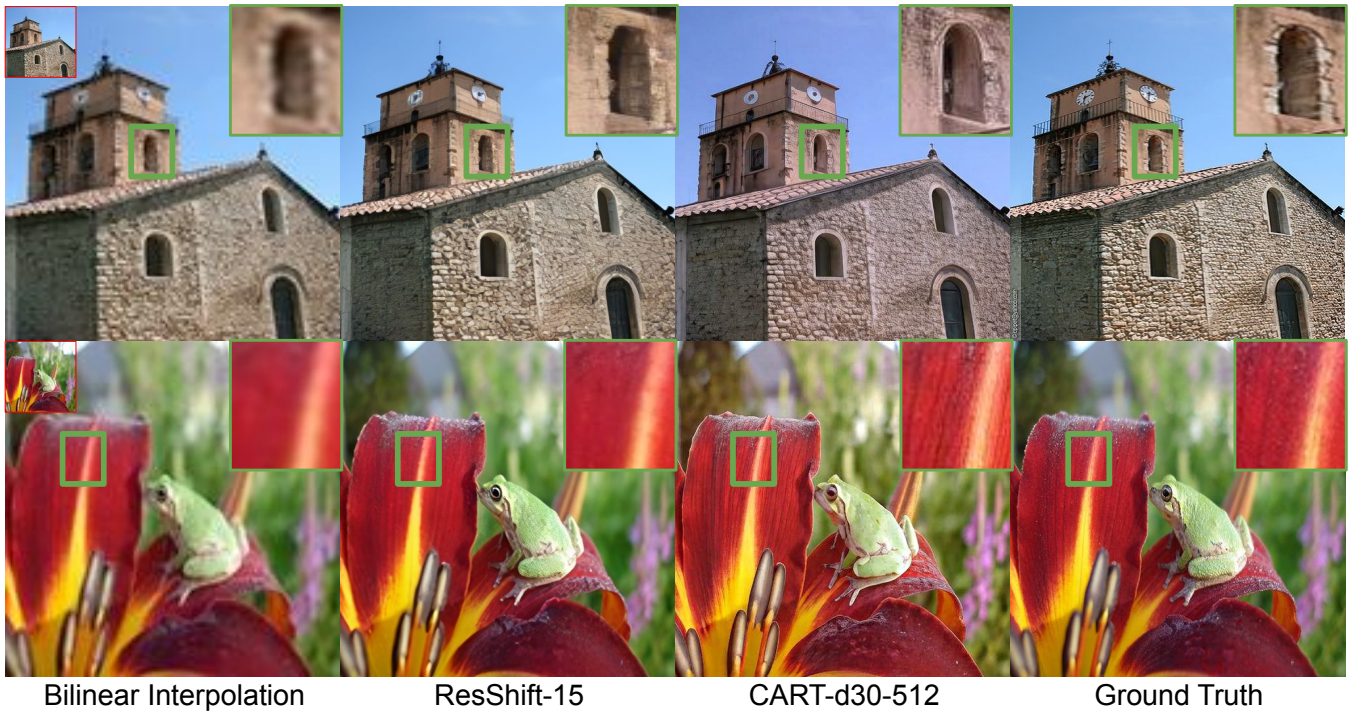


Figure 26: Comparison of CART for super-resolution with ResShift. Zoom-in recommended to observe finer details.

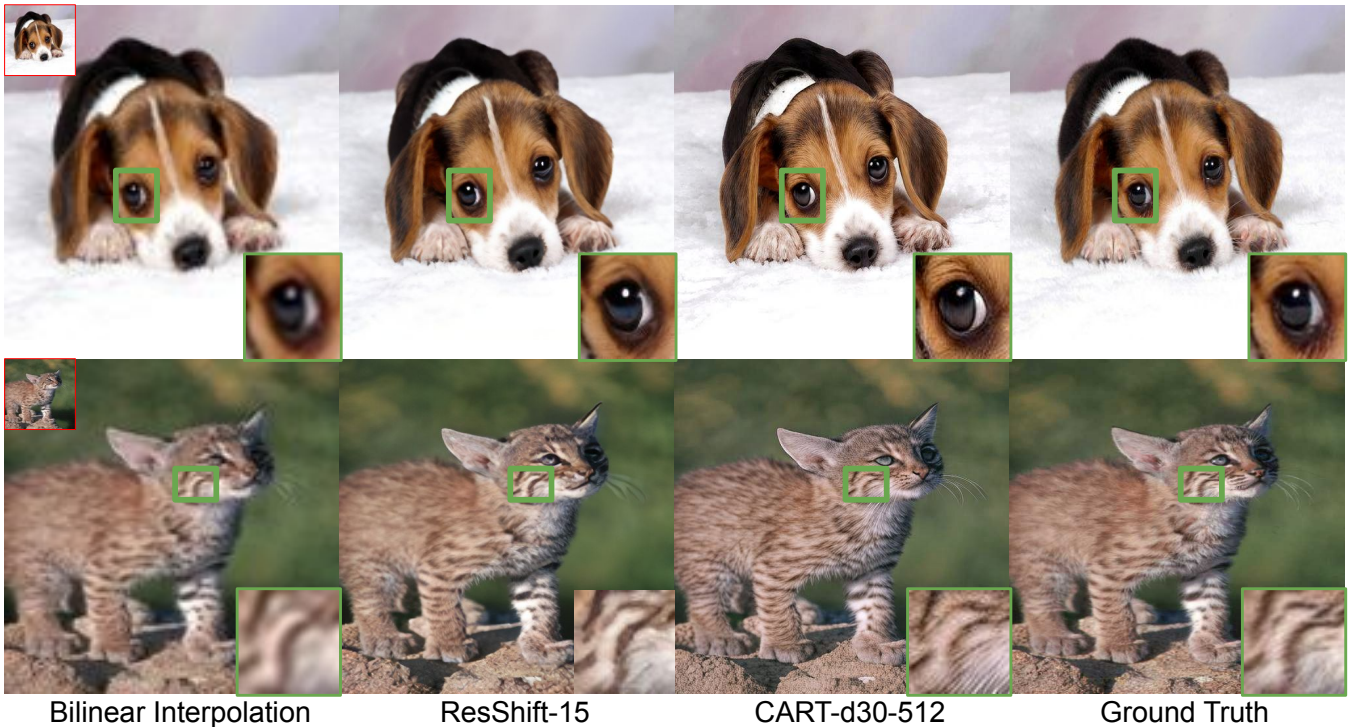


Figure 27: Comparison of CART for super-resolution with ResShift. Zoom-in recommended to observe finer details.

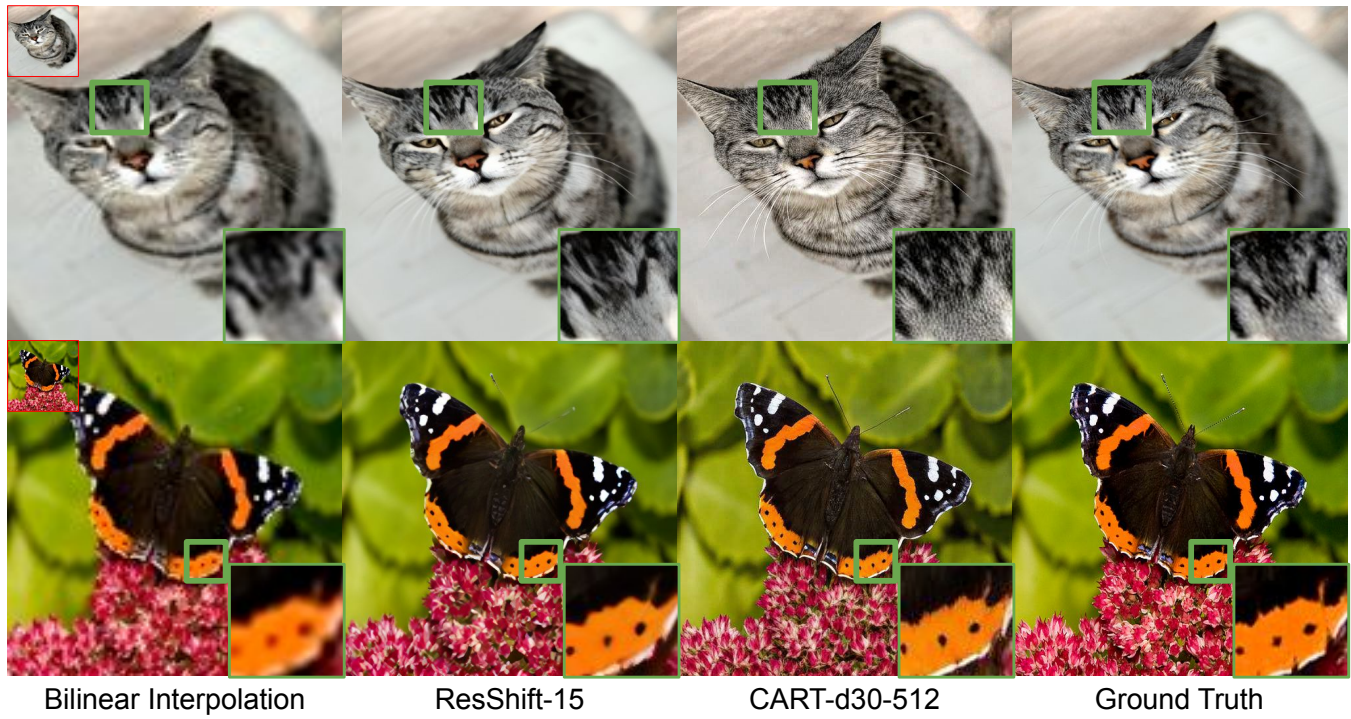


Figure 28: Comparison of CART for super-resolution with ResShift. Zoom-in recommended to observe finer details.

Specularity Decomposition for Illumination Control in Generated Images

Replacing the base-detail decomposition in Section with Specularity decomposition (Saini and Narayanan 2024) enables explicit control over lighting effects in the generated images. According to the dichromatic reflection model (Tominaga 1994) an image consists of a diffuse \mathbf{A} and a specular \mathbf{E} : $\mathbf{I} = \mathbf{A} + \mathbf{E}$. We employ a 4th-order decomposition, introducing four levels of illumination control, $\mathbf{I} = \mathbf{A}_4 + \mathbf{E}_4 + \mathbf{E}_3 + \mathbf{E}_2 + \mathbf{E}_1$. The generation process consists of 16 autoregressive steps, where the first 8 steps generate the base factor, and the subsequent 8 steps refine the image by incorporating controlled lighting variations. Figures 29-30 presents examples of images generated using Specularity decomposition, demonstrating the model’s ability to synthesize images with varying illumination while maintaining structural consistency.



Figure 29: Generation using specularity decomposition. Top row: Base diffuse term, 2nd – 5th rows: addition of specular terms to change illumination.

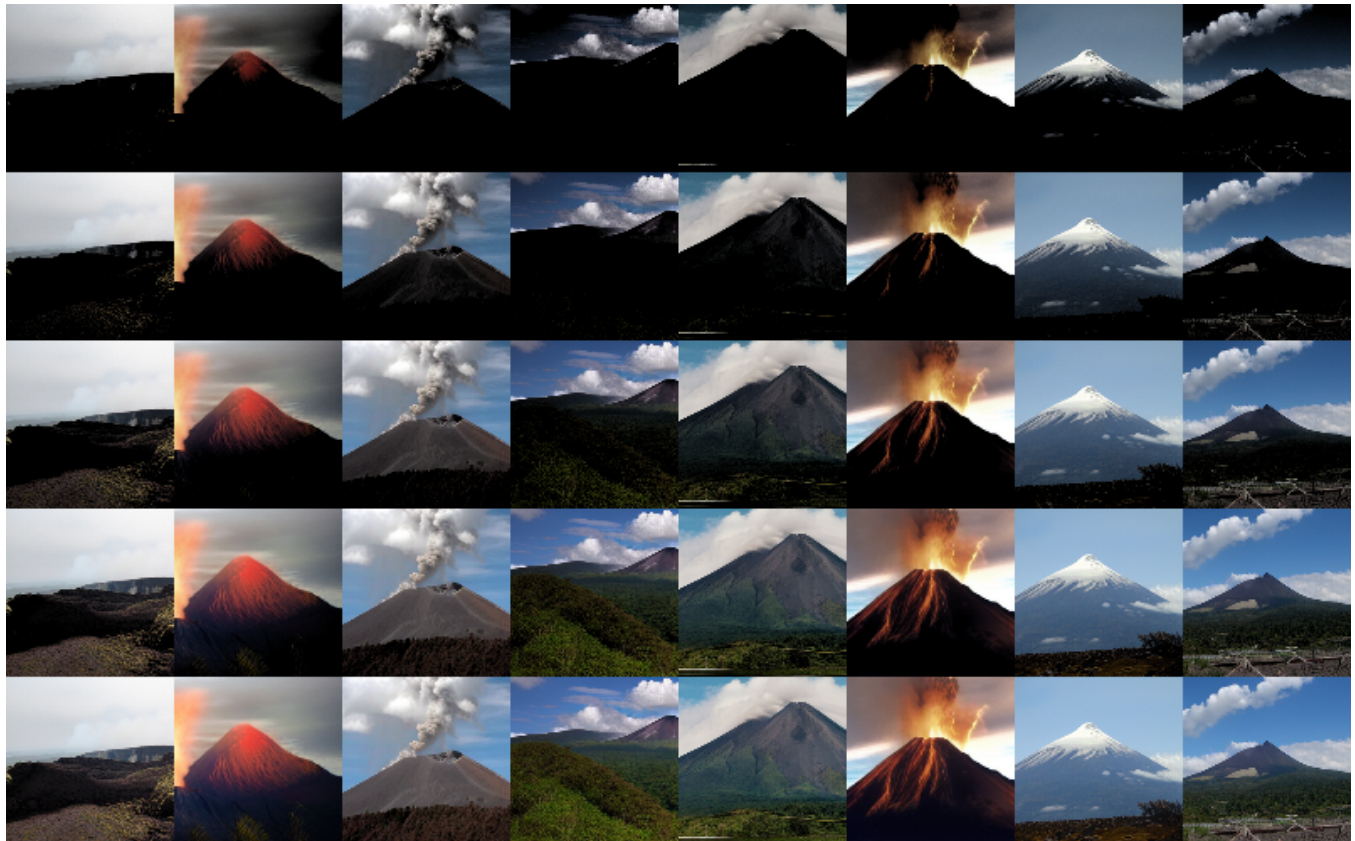


Figure 30: Generation using specularity decomposition. Top row: Base diffuse term, 2nd – 5th rows: addition of specular terms to change illumination.

Generative process and comparisons with VAR

Figures 31-32 presents a comparison of intermediate results and attention maps between CART and VAR, which utilizes multi-scale tokens. As discussed in Section , VAR simultaneously models both global and local features at each intermediate step, leading to an entangled representation of structure and texture. In contrast, CART first generates a smooth base image that captures only the global structure, followed by the progressive addition of fine details in later steps.

This hierarchical decomposition enables a clear separation of global and local features, facilitating high-resolution image synthesis and improving adaptability across different resolutions. Additionally, this tokenization strategy aligns more closely with human perception, where broad structures are recognized before finer details. Figures 33-38 illustrate the iterative refinement process in CART, where details are progressively introduced.

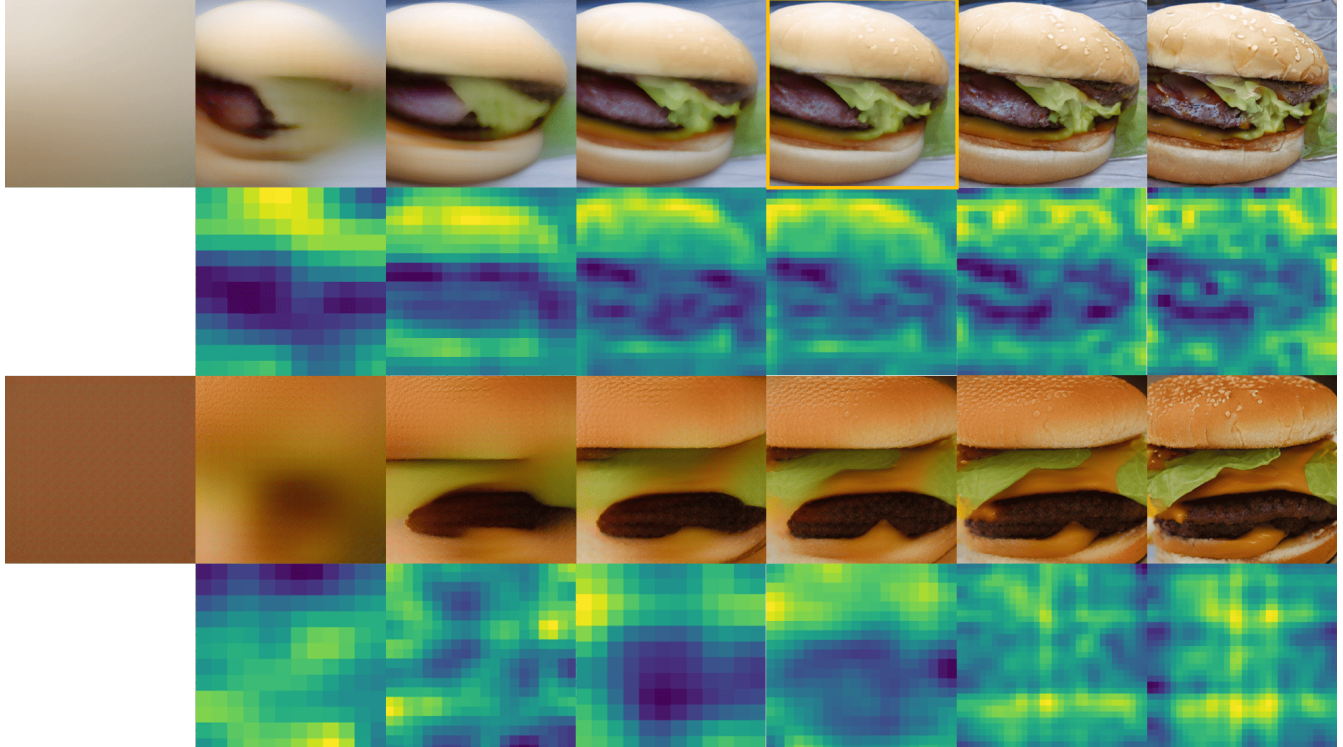


Figure 31: Top row: Intermediate visual results for CART. Base image is marked by yellow outline. 2nd row: Self-attention maps for corresponding intermediate layers of CART. 3rd row: Intermediate visual results for VAR. bottom row: Self-attention maps for corresponding intermediate layers of VAR.

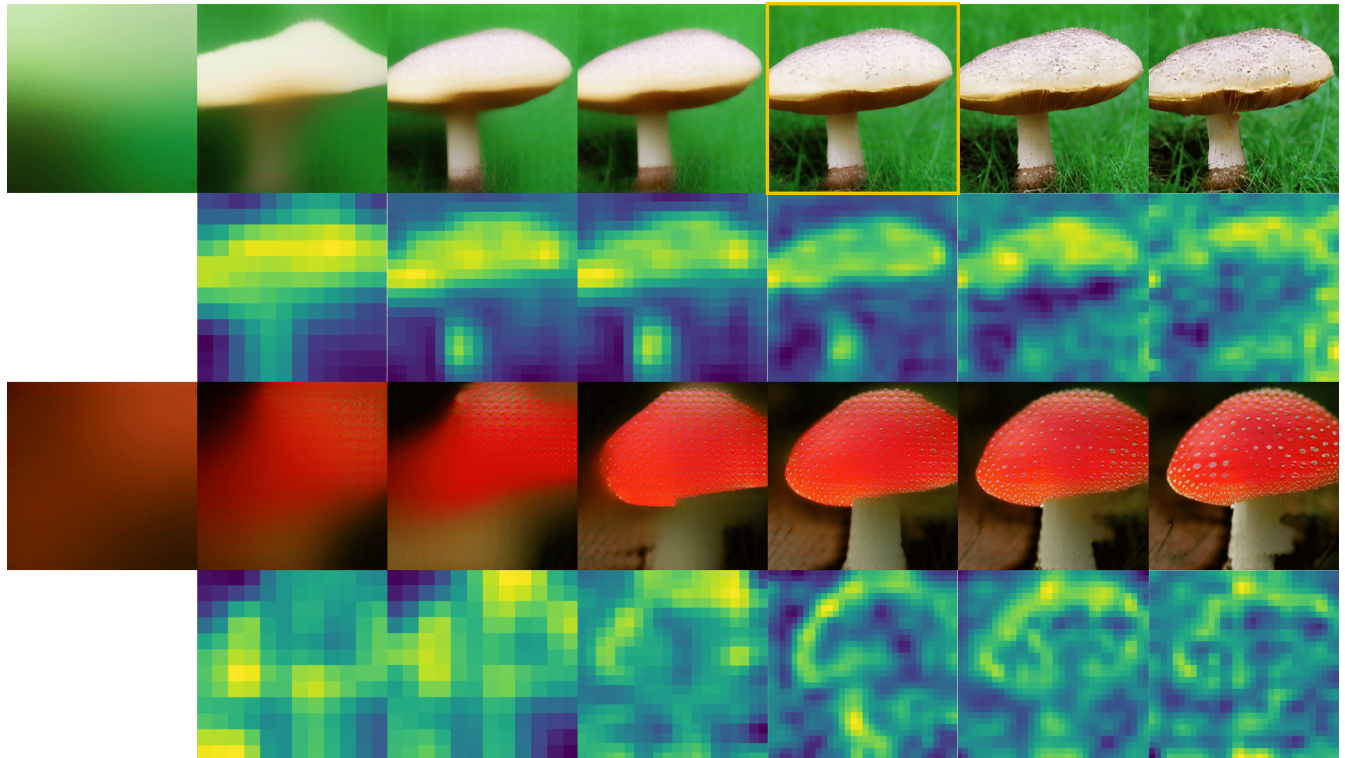


Figure 32: Top row: Intermediate visual results for CART. Base image is marked by yellow outline. 2nd row: Self-attention maps for corresponding intermediate layers of CART. 3rd row: Intermediate visual results for VAR. bottom row: Self-attention maps for corresponding intermediate layers of VAR.



Figure 33: Stepwise generation process (left to right) of samples in CART for bullet train, coffee cup, coffee pot, and monastery classes (top to bottom)

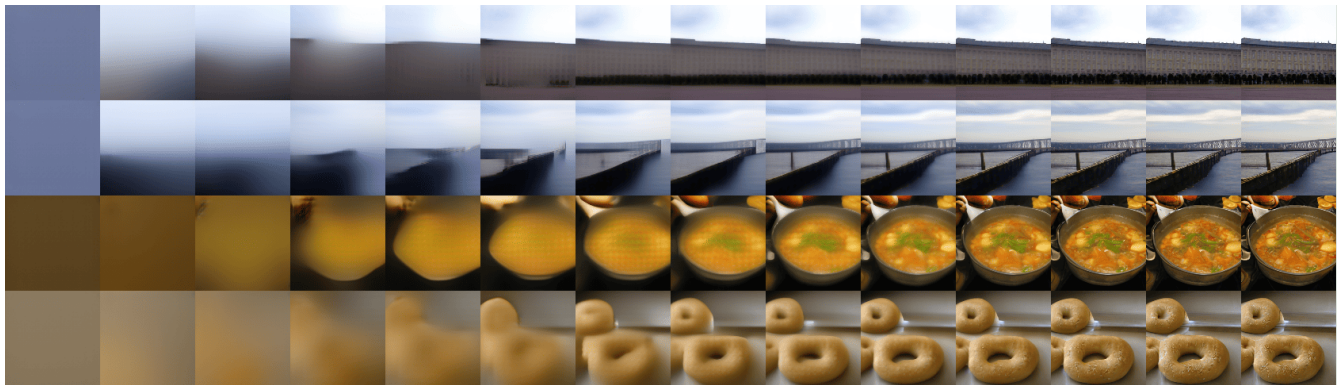


Figure 34: Stepwise generation process (left to right) of samples in CART for palace, pier, hotspot, and bagel classes (top to bottom)



Figure 35: Stepwise generation process (left to right) of samples in CART for strawberry, espresso, alps, and cliff classes (top to bottom)

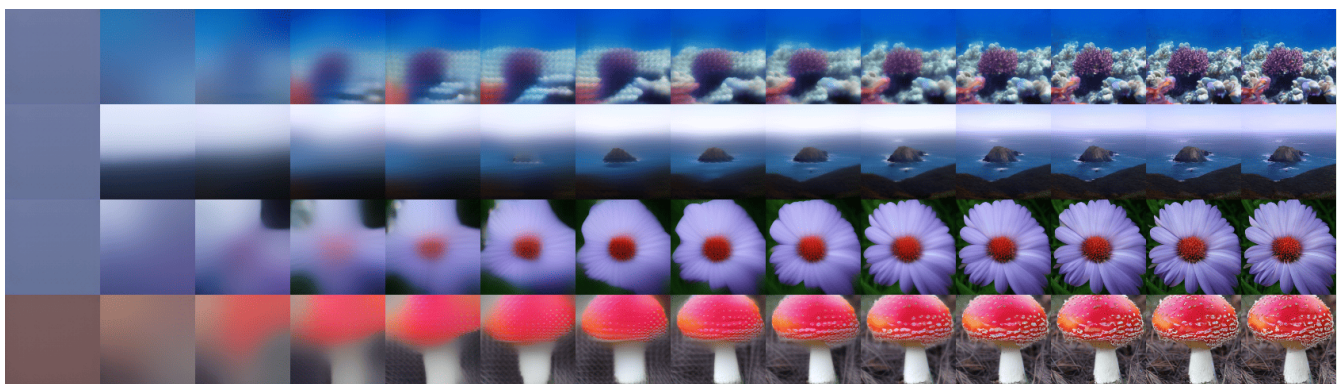


Figure 36: Stepwise generation process (left to right) of samples in CART for coral reef, foreland, daisy, and agaric classes (top to bottom)



Figure 37: Stepwise generation process (left to right) of samples in CART for geyser, lake, sandbar, and scuba diver classes (top to bottom)

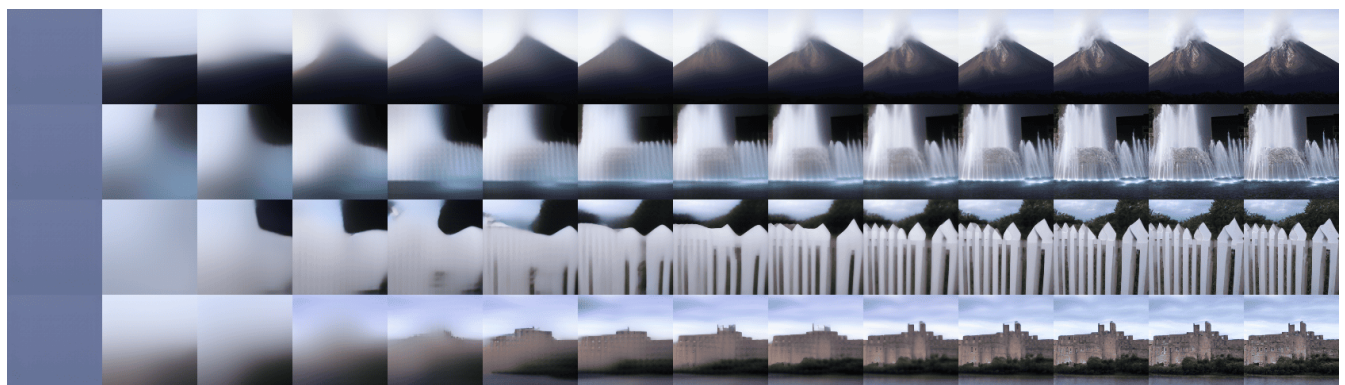


Figure 38: Stepwise generation process (left to right) of samples in CART for volcano, fountain, picket fence, and castle classes (top to bottom)